Cell

Mechanism of lipid transfer by bridge-like protein VPS13A and the scramblase XK

Graphical abstract

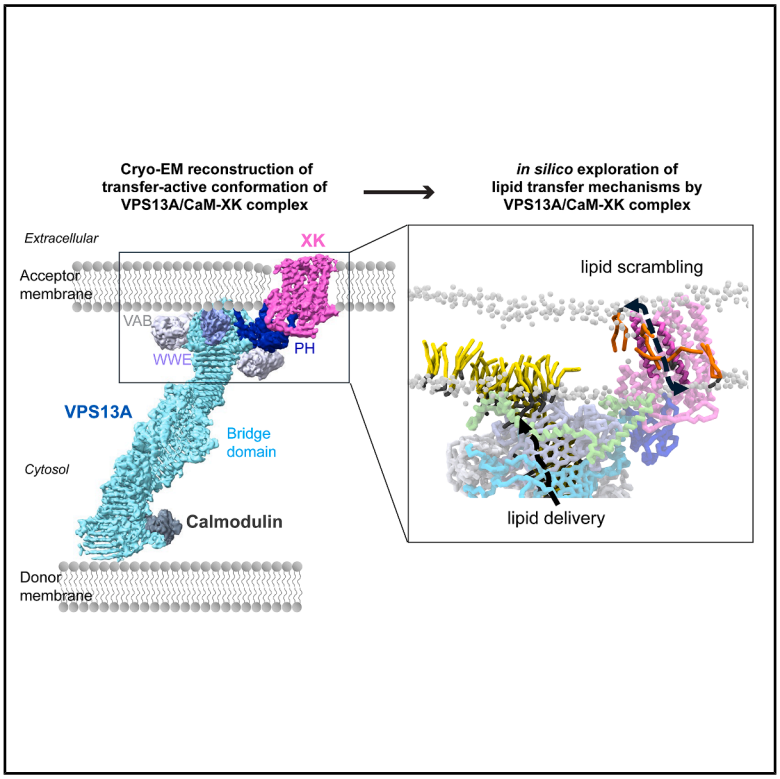

Highlights

- Complexed with XK, VPS13A can adopt a lipid-transfer active conformation
- Lipids are transferred from VPS13A's "bridge-domain" directly to membrane
- Overloading VPS13A's bridge-domain with lipids promotes robust bulk lipid transfer
- *In silico*, VPS13A association and membrane tension promote XK scrambling activity

Authors

Bodan Hu, Daniel Álvarez, Cristian Rocha-Roa, ..., Pietro De Camilli, Stefano Vanni, Karin M. Reinisch

Correspondence

stefano.vanni@unifr.ch (S.V.), karin.reinisch@yale.edu (K.M.R.)

In brief

The cryo-electron microscopy structure of the bridge-like lipid-transfer protein VPS13A in complex with the scramblase XK—coupled with molecular dynamics simulations—suggests that VPS13A-transported lipids are delivered from the protein directly to the membrane, near to the scramblase that equilibrates lipids between the membrane's leaflets as new lipids arrive.

Hu et al., 2026, Cell *189*, 1–15
August 6, 2026
https://doi.org/10.1016/j.cell.2026.05.027

CellPress

Please cite this article in press as: Hu et al., Mechanism of lipid transfer by bridge-like protein VPS13A and the scramblase XK, Cell (2026), https://doi.org/10.1016/j.cell.2026.05.027

Cell

CellPress
OPEN ACCESS

Article

Mechanism of lipid transfer by bridge-like protein VPS13A and the scramblase XK

Bodan Hu,[1,8] Daniel Álvarez,[2,3,8] Cristian Rocha-Roa,[2] Valentin Guyard,[2] Dazhi Li,[1] Yara Ahmed,[2] Xinbo Wang,[1,4,5,6] Pietro De Camilli,[1,4,5,6] Stefano Vanni,[2,7,*] and Karin M. Reinisch[1,9,*]

[1]Department of Cell Biology, Yale University School of Medicine, New Haven, CT, USA
[2]Department of Biology, University of Fribourg, 1700 Fribourg, Switzerland
[3]Department of Engineering, Universidad Loyola Andalucía, Avenida de las Universidades, Seville, Spain
[4]Department of Neuroscience, Yale University School of Medicine, New Haven, CT, USA
[5]Howard Hughes Medical Institute, Yale University School of Medicine, New Haven, CT, USA
[6]Program in Cellular Neuroscience, Neurodegeneration, and Repair, Yale University School of Medicine, New Haven, CT, USA
[7]Swiss National Center for Competence in Research Bio-Inspired Materials, University of Fribourg, 1700 Fribourg, Switzerland
[8]These authors contributed equally
[9]Lead contact
*Correspondence: stefano.vanni@unifr.ch (S.V.), karin.reinisch@yale.edu (K.M.R.)
https://doi.org/10.1016/j.cell.2026.05.027

SUMMARY

In eukaryotes, bridge-like lipid-transfer proteins (BLTPs) are central in mediating vesicle-independent lipid transfer between organelles. BLTPs span the cytosolic space between organelles at contact sites, featuring hydrophobic channels for lipids to travel between membranes. How BLTPs cooperate with partner proteins to orchestrate lipid delivery remains a mystery. Here, we used cryo-electron microscopy to visualize a complex comprising the prototypical BLTP VPS13A and the plasma membrane-localized scramblase XK at near-atomic resolution. VPS13A interacts with XK via its pleckstrin homology domain, priming VPS13A's bridge-like lipid-transfer domain to deliver lipids directly to the cytosolic leaflet of the acceptor membrane. In molecular dynamics simulations, this arrangement allows for robust lipid transfer. Newly delivered lipids can then be equilibrated between leaflets of the membrane bilayer by the scramblase, allowing for membrane growth. Mechanistic insights regarding lipid delivery by VPS13A are directly applicable to all VPS13 proteins and, more broadly, to all BLTP family members.

INTRODUCTION

In eukaryotes, the lipids that constitute organellar membranes are synthesized primarily in the endoplasmic reticulum (ER) before being redistributed to other organelles. While it has long been known that lipid transfer between intracellular membranes can take place via vesicular trafficking, it is now appreciated that bridge-like lipid-transfer proteins (BLTPs) play a central and fundamental role in bulk lipid movement, independent of vesicles. BLTPs span between organelles at sites of close apposition via a "bridge-domain," featuring a hydrophobic groove along which lipids can flow between organellar membranes.[1]

BLTP-mediated bulk lipid transfer is now believed to be key in membrane expansion accompanying the biogenesis of new organelles like the autophagosome[2]; membrane maintenance for organelles outside vesicle trafficking pathways like mitochondria[3]; or membrane repair, for example, of damaged lysosomal membranes.[4] The founding members of the BLTP family, the VPS13 proteins, are also of great biomedical interest because their dysfunctions underlie neurological diseases such as Parkinson's disease (VPS13C) or chorea-acanthocytosis (VPS13A), and along with the ATG2 family that functions in autophagy, they are the most studied BLTPs.[1,5]

An emerging paradigm—based primarily on studies of VPS13 and ATG2 proteins[6–9]—is that at the acceptor membrane, BLTPs cooperate with membrane-embedded scramblases, proteins that equilibrate phospholipids between membrane leaflets; this cooperation allows for the concomitant expansion of both leaflets of the membrane, even though the BLTP delivers lipids to only one leaflet. The mechanisms governing the transfer of lipids from the bridge-domain to the membrane and the role of the scramblase in this process have been elusive in the absence of near-atomic resolution information regarding BLTP-scramblase complexes.

Here, we combine structural and computational approaches to investigate how a member of the VPS13 family, human VPS13A, partners with a plasma membrane scramblase in the XK-related family, called XK or XKR1, for lipid delivery. Loss-of-function mutations in VPS13A result in chorea-acanthocytosis, a Huntington-like neurodegenerative condition accompanied by abnormal red cells in the blood (acanthocytes).[10] A very similar condition, called McLeod's syndrome, is caused

Please cite this article in press as: Hu et al., Mechanism of lipid transfer by bridge-like protein VPS13A and the scramblase XK, Cell (2026), https://doi.org/10.1016/j.cell.2026.05.027

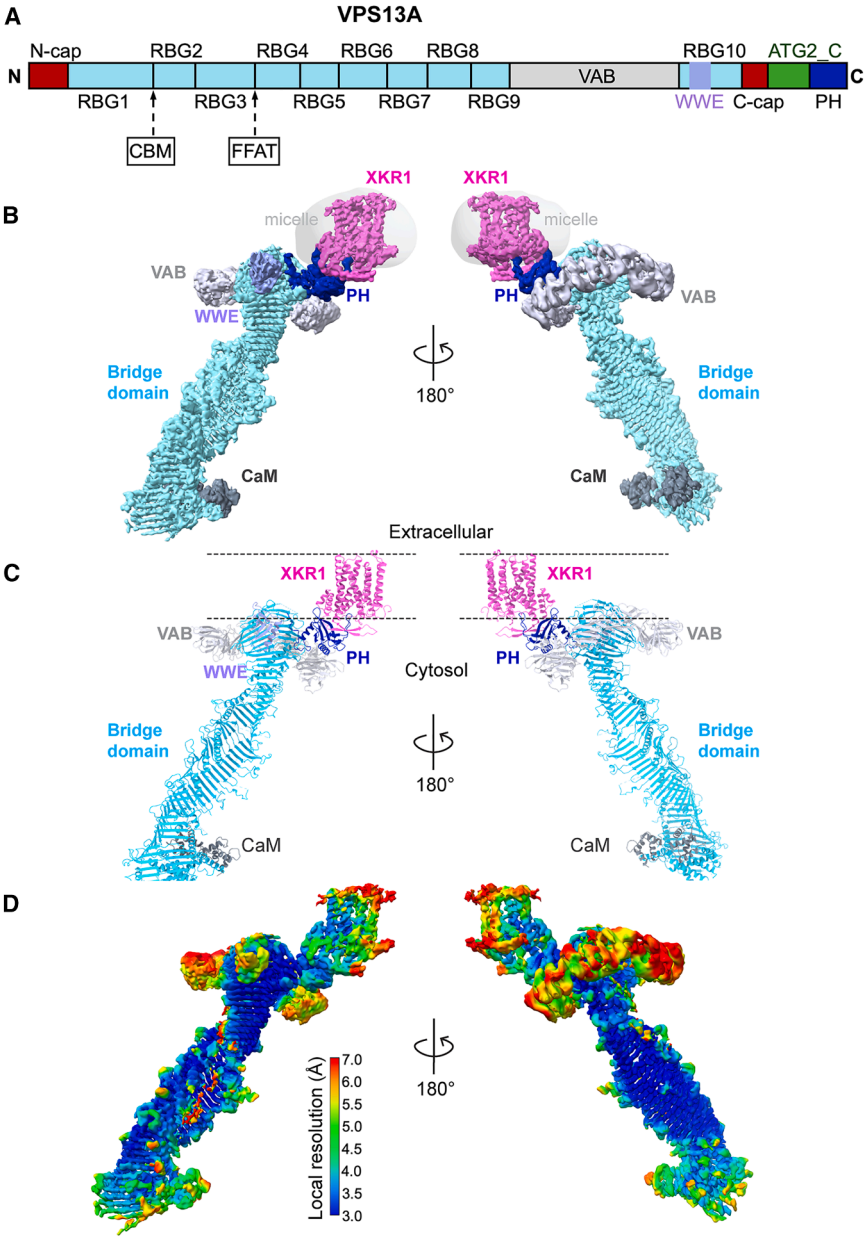

Figure 1. Architecture of the VPS13A/CaM-XKR1 complex

(A) Schematic of VPS13A domain architecture. CBM, calmodulin binding motif; FFAT, peptide motif involved in VPS13A-ER association.

(B) Cryo-EM map of the VPS13A/CaM-XKR1 complex, with the membrane protein XKR1 embedded in GDN micelle. Color coding for VPS13A is as in (A); XKR1 is pink, and CaM is slate gray.

(C) Model of the VPS13A/CaM-XKR1 complex, shown in the same color and orientation as the map in (B).

(D) Local resolution of cryo-EM map of the VPS13A/CaM-XKR1 complex, shown in the same orientation as in (B).

See also Figures S1 and S2.

by loss-of-function mutations in XKR1,[11] consistent with a functional partnership and reported direct interaction between the two proteins.[12,13] Moreover, VPS13A and XKR1 were top hits in a screen for genes required for surface exposure of phosphatidylserine in T cells,[13] suggesting a model according to which VPS13A delivers phospholipids from the ER to the plasma membrane, where XKR1 scrambles them.[14] VPS13A also localizes to other sites in the cell, such as contacts between the ER and mitochondria, where its function is less well investigated.[15]

We used cryo-electron microscopy (cryo-EM) to visualize the complex of VPS13A, a recently identified soluble interaction partner calmodulin (CaM),[16] and detergent solubilized XKR1 at near-atomic resolution (3.28–3.41 Å, in three different maps). The interaction between VPS13A and XKR1 orients the VPS13A bridge-domain in the direct vicinity of the lipid bilayer, and it pins VPS13A close to the scramblase. Molecular dynamics (MD) simulations show that the cryo-EM structure is compatible with robust direct lipid transfer between the bridge-domain and the cytosolic leaflet of the acceptor membrane, hinting that membrane properties, such as membrane tension, might couple lipid delivery with lipid scrambling by XKR1. We expect that the mechanistic insights regarding lipid delivery by VPS13A described here are directly applicable to all VPS13 and ATG2 proteins, as well as, more broadly, other BLTP families.

RESULTS

VPS13A/CaM-XKR1 complex preparation, cryo-EM single-particle reconstruction, and modeling

We separately produced FLAG-tagged human XKR1 (3XFLAG-XKR1) and VPS13A (VPS13A-3XFLAG) by transfection into Expi293 cells. XKR1 was isolated from the glyco-diosgenin (GDN)-solubilized membrane fraction via affinity purification using an anti-FLAG resin; similarly, VPS13A was sequestered from the soluble fraction in the absence of detergent, co-purifying with a recently identified interaction partner CaM[16] (Figure S1). XKR1 and VPS13A/CaM were mixed, and the ensuing complex was isolated by size-exclusion chromatography and then subjected to cryo-EM single-particle analysis (Figure S2A). We generated two maps, one for VPS13A/CaM and another centered on XKR1 and the VPS13A PH domain. Local refinement yielded a series of maps with nominal resolutions ranging from 3.28 to 3.41 Å (Figures 1 and S2B). The maps allowed us to model most of the VPS13A/CaM-XKR1 complex at near-atomic resolution. The portions of VPS13A visualized include most of the bridge-domain as

Please cite this article in press as: Hu et al., Mechanism of lipid transfer by bridge-like protein VPS13A and the scramblase XK, Cell (2026), https://doi.org/10.1016/j.cell.2026.05.027

well as C-terminal adaptor modules responsible for its attachment to acceptor membranes: the VPS13 adaptor binding (VAB) (poorly resolved), tryptophan-tryptophan-glutamate (WWE) (poorly resolved), and pleckstrin homology (PH) "adaptor" domains (Figure 1). Density for CaM was also well defined. Amphipathic helices at the membrane-proximal end of the bridge-domain, conserved across all VPS13s and ATG2 proteins (and referred to as the ATG2_C region for their location at the C terminus of ATG2; Figure 1A), are not visible in the reconstruction, and they were not modeled. The taco-shell-shaped bridge-domain comprises a series of 10 repeating-β-groove (RBG) modules[17] arranged end to end and sandwiched between N- and C-terminal "caps." Each RBG module consists of five highly curved, antiparallel β strands and connecting segments, whose concave surface is lined entirely by hydrophobic residues and thus suited to solubilize lipid fatty acid moieties. To model the bridge-domain, we segmented an AlphaFold-generated model[18] of the bridge-domain into RBG modules and rigid-body fitted the RBG fragments into the experimental maps (Figure S2C). We similarly placed AlphaFold-generated coordinates for XKR1 and adaptor domains of VPS13A (VAB, WWE, and PH domains) and CaM into the maps. Once the initial model was assembled, we combined artificial intelligence-based map interpretation in DeepMainMast, rigid body fitting in ChimeraX, and manual rebuilding in COOT to construct a final model.[19–21] Except for the VAB and the bridge-domain caps in the lowest-resolution parts of the reconstruction, the model was subjected to real space refinement in Phenix.[22] (See Table S1 for data collection and model statistics and Figure S2D for representative density.)

Overview of the complex

At low resolution, VPS13A resembles a bubble wand (Figures 1B–1D). It comprises the elongated bridge-domain, serving as the bubble wand's "handle," and the C-shaped VAB domain emanating from it, which is prominent as the largest of the adaptor domains and corresponds to the bubble wand's "loop." The VAB and the smaller PH and WWE domains are arranged in a plane encircling the C-terminal end of VPS13A's bridge-domain, all positioned to interact with the acceptor membrane and/or membrane-embedded receptors like XKR1. CaM binds to the N-terminal end of the bridge-domain (Figure S1).

VPS13A connects to the detergent-micelle-embedded XKR1 via its C-terminal end. The WWE and VAB adaptor domains are not required for VPS13A's interaction with XKR1 or VPS13A's recruitment to the plasma membrane,[14] and accordingly they do not contact XKR1. VPS13A interacts with detergent-solubilized XKR1 solely via its PH adaptor domain, which protrudes rigidly from the back of the taco-shell-shaped bridge-domain (Figures 1B and 1C). The PH domain is positioned over XKR1 in the membrane and does not appear to access the membrane directly, except that two loops—PH-$L_{\beta3\text{-}\beta4}$ and PH-$L_{\beta6\text{-}\beta7}$—independently interact with residues of XKR1 transmembrane (TM) helices (see below).

Importantly, there is no direct interaction between the bridge-domain of VPS13A and XKR1; and the bridge-domain, whose long axis is tilted ∼35° from a normal to the membrane plane as defined by the micelle surface, is positioned to deliver lipids directly to the acceptor membrane (Figures 1B and 1C).

VPS13A bridge-domain and bound lipids

As expected from AlphaFold predictions, the bridge-domain forms an ∼240-Å-long extended β sheet with a taco-shell-shaped structure, whose interior is lined by hydrophobic residues to form the lipid transport groove and whose exterior is hydrophilic (Figure 2). In the experimental structure, the taco shell twists by 270° over its length. The width and depth of the lipid-transfer groove vary along the length of VPS13A. The width across the groove ranges from ∼25 Å across at its widest points near the ends to ∼9 Å across at its narrowest points (Figures 2A and 2B), just wide enough across to accommodate one to two lipids. The width across other experimentally characterized VPS13s (VPS13C and fungal VPS13[16,23]) and BLTPs (BLTP1 and ATG2[24,25]) is similarly variable. Whether this variability is relevant for the transfer mechanism is not known, although it is intriguing to speculate that modulating channel width could regulate lipid flow rates.

The lipid-transfer groove of VPS13s can accommodate tens of glycerophospholipids.[26] Based on previous mass spectrometry analyses of the lipids that co-purify with fungal Vps13 or human ATG2A,[15,27] the bound lipids are glycerophospholipids, with varying acyl chain and head group compositions. The reconstruction represents an average of ∼0.4 million VPS13A/CaM-XKR1 complexes, so that the density for lipids in the transfer groove is also averaged. Nevertheless, we observed density interpretable as lipid in the best resolved parts of the bridge-domain in RBG3–RBG10 (Figures 2C and 2D). In particular, we can resolve rows of fatty acyl moieties along the hydrophobic walls of the taco shell, indicating that there are distinct sites for binding fatty acyl chains within the bridge-domain. The corresponding head groups, which are expected to be solvent exposed at the top of the taco shell, as well as lipid tails in the middle of the transfer channel away from the walls are not resolved in the maps.

The cap regions at either end of the bridge-domain (Figure 2A) are poorly defined in the maps of the VPS13A/CaM-XKR1 complex, reflecting high mobility, and we cannot confidently model them (Figure 1D). The VAB domain is also mobile, as reflected by the low resolution in corresponding parts of the map (Figure 1D). The particles used for reconstruction can be separated into different 3D classes, showing the VAB domain in a continuum of conformations (Figures 2E and 2F), and its position in the model represents an average of these conformations. In the model, the VAB domain is positioned at side of the bridge-domain, allowing the bridge-domain to connect to the acceptor membrane, in a "transfer-permissive" conformation. Notably, though, in the reconstruction of another VPS13 alone (VPS13C),[16] not in complex with a membrane receptor like XKR1, the VAB domain is in a "transfer-incompatible" conformation, arching over the bridge-domain to prevent its connection to the membrane. In contrast to the C-terminal cap in VPS13A, the cap in VPS13C is well defined in the 3D reconstruction, showing that linker segments between the cap's β strands interact with the VAB to maintain it in the transfer-inactive conformation. In the VPS13C structure (and in AlphaFold predictions for VPS13A), two α helices in the cap (residues 2,799–2,810 and 2,839–2,860 in VPS13A) partially obstruct the lipid-transfer channel. 3D variability analysis of the particles used in the

Please cite this article in press as: Hu et al., Mechanism of lipid transfer by bridge-like protein VPS13A and the scramblase XK, Cell (2026), https://doi.org/10.1016/j.cell.2026.05.027

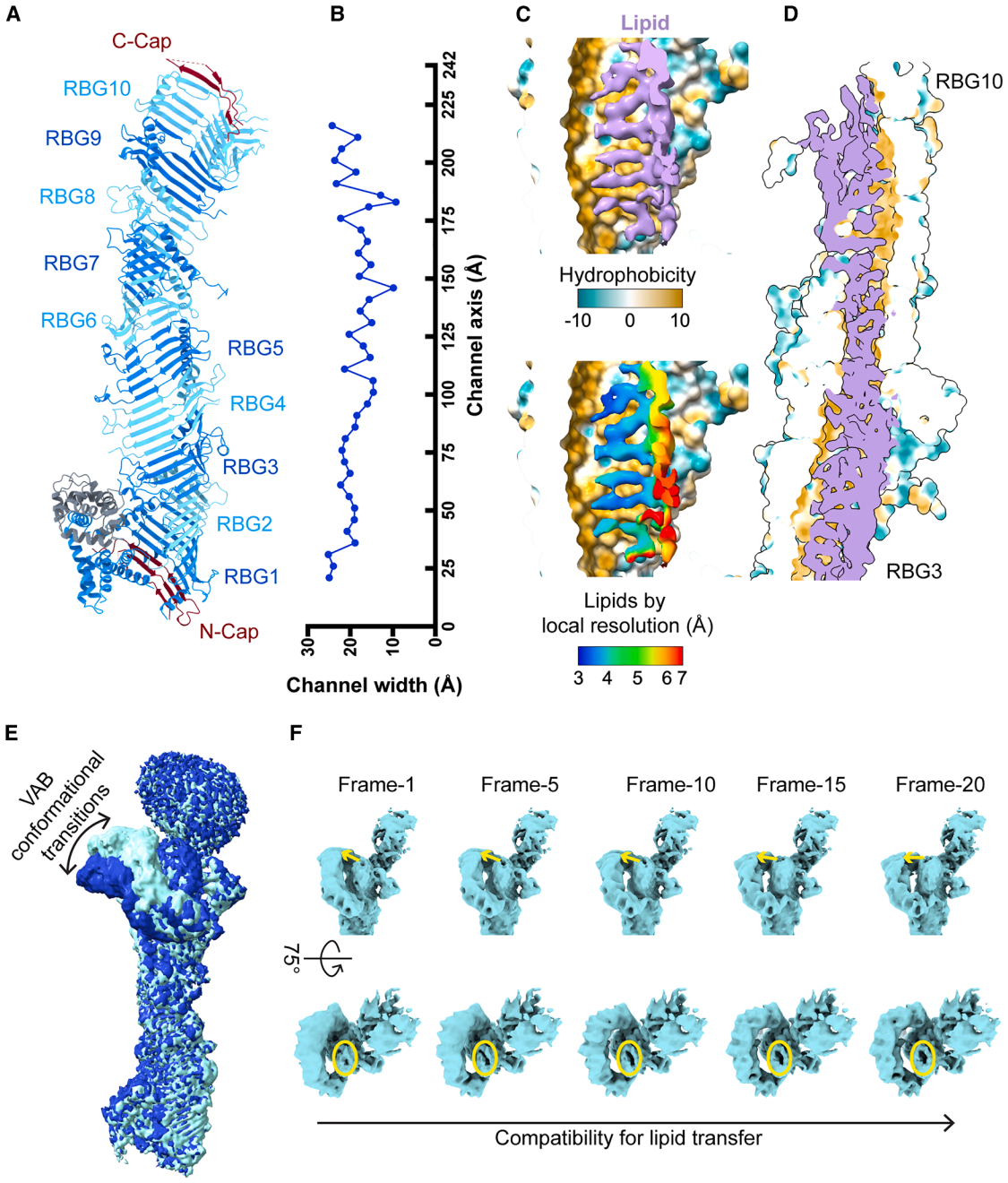

Figure 2. Structure, lipid binding, and conformational dynamics of the VPS13A bridge-domain

(A) The bridge-domain comprises 10 repeating-β-groove (RBG) motifs shown in blue; modeled portions of the cap regions located at the N and C termini of the lipid-transfer channel are in maroon.

(B) Width of the lipid-transfer channel calculated using ChimeraX, excluding the N-terminal and C-terminal cap regions from analysis.

(C) Cross-section view of the hydrophobic cavity of RBG3 and RBG4, in space filling representation, showing density corresponding to lipids in the cryo-EM maps. Local resolution of lipid density is shown in the lower panel.

(D) Cross-section view of the bridge-domain, highlighting the presence of lipids within the channel spanning from RBG3–RBG10.

(E) Representative cryo-EM maps of the VPS13A/CaM-XKR1 complex obtained from 3D classification, illustrating conformational changes in the VAB domain. The VAB adopts a continuum of conformations; the conformation shown in dark blue is more compatible with lipid transfer.

(F) Representative frames from 3D variability analysis illustrating the coordinated movement of the VAB and C-terminal cap of VPS13A. Shifts in the VAB domain from above to the side of the bridge-domain (yellow arrows in the top panel) are accompanied by opening of the cap (yellow circle in the bottom panel) as VPS13A adopts a lipid-transfer compatible conformation.

Please cite this article in press as: Hu et al., Mechanism of lipid transfer by bridge-like protein VPS13A and the scramblase XK, Cell (2026), https://doi.org/10.1016/j.cell.2026.05.027

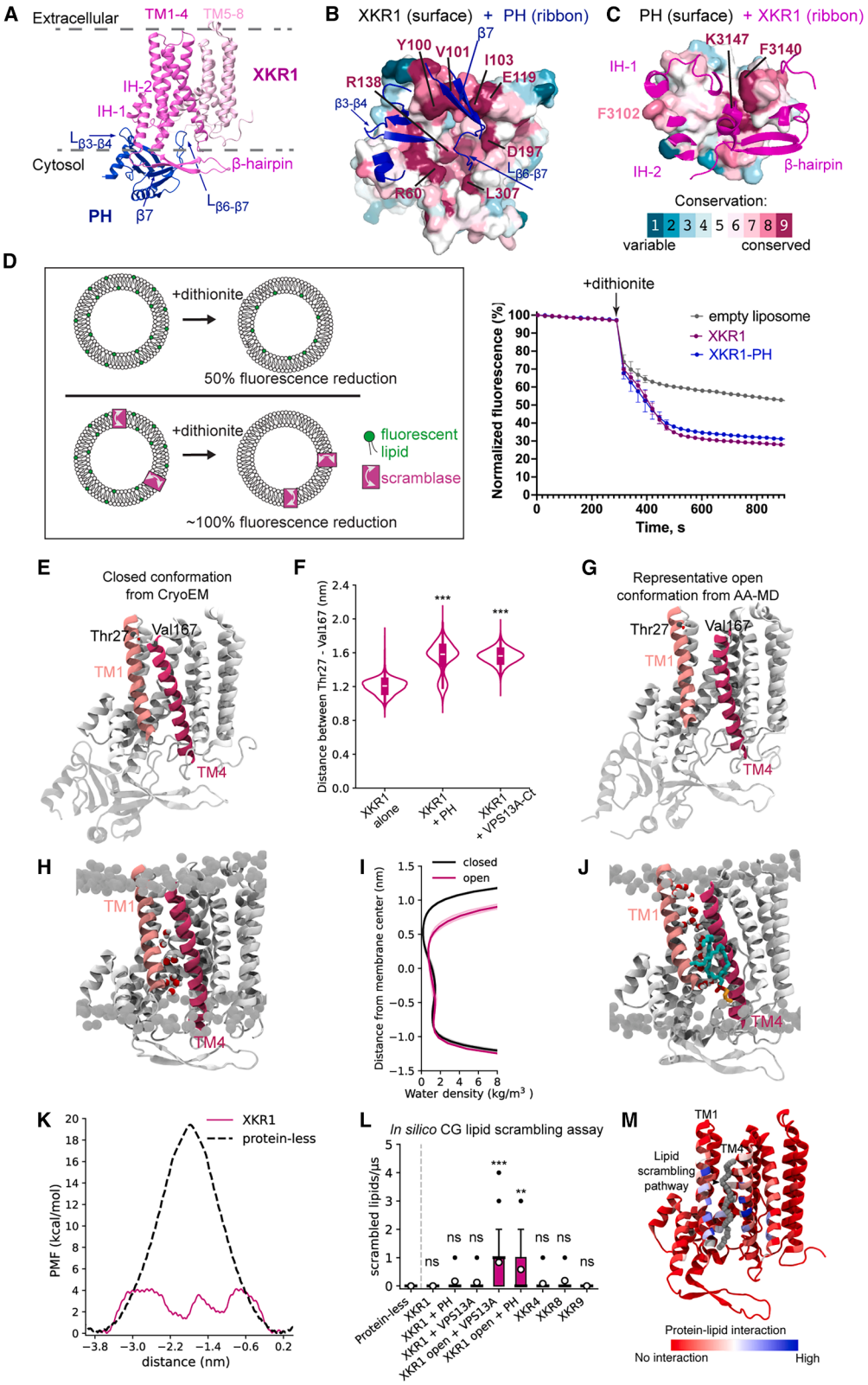

(legend on next page)

Please cite this article in press as: Hu et al., Mechanism of lipid transfer by bridge-like protein VPS13A and the scramblase XK, Cell (2026), https://doi.org/10.1016/j.cell.2026.05.027

reconstruction of the VPS13A/CaM-XKR1 complex reveals a coordinated movement of densities corresponding to the VAB and the cap in the transition between conformations (Figures 2E and 2F). The rearrangements in the cap are consistent with a potential role in facilitating lipid exit from the bridge-domain (Figure 2F). We propose that as VPS13s engage with the acceptor membrane and receptors there, their VAB adjusts from a lipid-transfer inactive conformation, where the C-terminal cap is ordered, to a transfer-active conformation, in which the cap rearranges to engage with membrane for lipid delivery. Likewise, we expect that the N-terminal cap could undergo structural changes as it engages with the donor membrane. Given the transfer-active and -inactive conformations of the VAB observed in our structure here and the VPS13C structure,[16] respectively, we propose that VPS13 activity in cells could be regulated via the transition between conformations that differ in the position of the VAB vis-à-vis the bridge-domain.

Finally, we observed density that could not be accounted for by VPS13A alone in maps for its N-terminal end. Based on studies with other VPS13 proteins, this density corresponds to CaM,[16] which co-purifies with VPS13s, including VPS13A (Figure S1). The CaM binding site on VPS13s is near the end of the bridge-domain that interacts with the ER, raising the possibility that CaM may be an exogenous adaptor for ER association.[16]

Architecture of XKR1

Experimental structures of XK-related proteins (XKR4, XKR8, and XKR9) have been reported before.[28–30] Consistent with these structures and AlphaFold predictions,[18] XKR1 comprises two modules, each consisting of four TM helices (TM1–TM4 in module 1; TM5–TM8 in module 2) and "inter-helices" (IH1 and IH2 in module 1; IH3 in module 2), which dip into but do not extend the whole distance through the lipid bilayer (Figure 3A).

XKR1 and all XK-related proteins feature a hydrophilic pocket facing the cytosolic surface of the membrane (Figure 3B). In XKR1, the pocket is partially covered by a β hairpin between IH2 and TM3 (Figures 3A–3C), which is not present in most other family members. Residues at the surface of the pocket, including in the β hairpin in the case of XKR1, are highly conserved, indicating functional significance as discussed further below.

Interaction between VPS13A and XKR1

On its cytosolic side, XKR1 binds VPS13A exclusively via the conserved pocket (including the overlaying β hairpin) that interacts with the PH domain of VPS13A through an extensive occluded surface area (~2,500 Å^2, including the surfaces in both VPS13A and XKR1) (Figure 3B). PH domain residues at the interface are also conserved. The PH domain may be described as a sandwich of two antiparallel β sheets, comprising strands 1–4 and 5–7, followed by a helix. Strand 7 of the PH domain associates with the XKR1 β hairpin, extending the PH domain's C-terminal β sheet. This interaction positions the PH domain directly over XKR1's conserved pocket and was previously shown to be essential for VPS13A targeting to the plasma membrane.[14,32] Further, loop PH-$L_{\beta3\text{-}\beta4}$ of the PH domain is in the micelle, inserted between IH1 and IH2 of XKR1 adjacent to the conserved surface pocket, via a phenylalanine residue, F3102, at its tip (Figures 3A–3C). F3102 is sandwiched between a

Figure 3. Lipid scrambling by XKR1-PH$_{(VPS13A)}$ complex

(A) Model of the XKR1-PH$_{(VPS13A)}$ complex as embedded in the plasma membrane. TM1–TM4 and TM5–TM8 in XKR1 are shown in dark and pale pink, respectively, and VPS13A's PH domain is dark blue. The interaction region between XKR1 and the PH domain is indicated.

(B) Surface view of XKR1 viewed from the cytosol; PH domain segments at the interface with XKR1 are in ribbon representation. The β hairpin and the cytosol accessible pocket are highly conserved.

(C) Surface view of the PH domain as seen from XKR1. XKR1 segments at the interface with the PH domain are in ribbon representation. Key conserved residues at the XKR1:PH domain interface are labeled. Conservation scores of residues of the PH domain (B) and XKR1 (C) were analyzed via Consurf (https://consurf.tau.ac.il/consurf_index.php).

(D) *In vitro* lipid scrambling assay, with schematic illustration on the left, shows that the XKR1-PH fusion protein demonstrated lipid scrambling activity comparable to XKR1 alone. Data of one representative experiment are shown as mean ± SD. Samples were analyzed in triplicate, and three independent experiments were performed with similar results.

(E) XKR1-PH$_{(VPS13A)}$ complex in a closed conformation as based on the cryo-EM reconstruction. The TM helices 1 and 4 from XKR1 are shown in light pink and pink ribbons, respectively. The rest of the protein and the PH domain are shown in gray.

(F) Distance between the Cα atoms from the residues Thr27 and Val167, located at the extracellular side of the TM1 and TM4, respectively, as measured in unbiased AA-MD simulations for the following systems: XKR1 alone, XKR1 + PH domain of VPS13A, XKR1 + VPS13A C-terminal region (residues 1,592–3,169). One-way ANOVA with Tukey's multiple comparison test; $^{***}p \leq 0.001$.

(G) Representative snapshot of the XKR1-PH$_{(VPS13A)}$ complex in an open conformation from unbiased AA-MD simulations, using the same color scheme as in (E).

(H) Representative snapshot of the hydrated closed XKR1 conformation.

(I) Water density profile along XKR1 for the closed (black) and open (pink) conformations.

(J) Representative snapshot of the open XKR1 conformation showing a lipid located at the cytosolic entrance of the cavity/interface between TM1 and TM4. The lipid tails are shown as cyan sticks, phosphate atoms in red, and choline atoms are in orange. The protein is colored as in (E).

(K) Free energy profile from AA-MD simulations for phospholipid translocation across a lipid bilayer in the presence of open XKR1 (pink line) and in the absence of protein (black dashed line). Data for the protein-less profile were taken from Bartoš et al.[31] For the XKR1 profile, the *x* axis shows the distance between the nitrogen atom of the head group of a selected lipid and the center of mass of four amino acids located on the extracellular side of the protein (see STAR Methods). The protein-free profile was aligned with the XKR1 profile for visual comparison.

(L) *In silico* CG-MD lipid scrambling assay for experimentally available structures of XK-related proteins and the open conformation obtained from the AA-MD simulations. One-way ANOVA with Tukey's multiple comparison test; $^{***}p \leq 0.001$, $^{**}p \leq 0.01$; ns: $p > 0.05$.

(M) Key residues involved in lipid scrambling in CG-MD simulations for the open conformation of XKR1. The averaged lipid scrambling pathway is shown as a continuous stalk of gray spheres. The red (no interaction)-blue (high interaction) color code indicates the interaction between each amino acid and the scrambled lipids.

See also Figure S3.

Please cite this article in press as: Hu et al., Mechanism of lipid transfer by bridge-like protein VPS13A and the scramblase XK, Cell (2026), https://doi.org/10.1016/j.cell.2026.05.027

leucine (L68) and a phenylalanine (F81) of XKR1 IH1 and IH2, respectively. A mutant construct in which the sequences in PH-domain β strands 3 and 4 and PH-$L_{\beta3\text{-}\beta4}$ were replaced with the corresponding sequences from VPS13C resulted in the PH domain's mistargeting, consistent with functional importance.[14] And finally, intriguingly, the loop between strands 6 and 7 of the PH domain (PH-$L_{\beta6\text{-}\beta7}$) extends into XKR1's conserved surface pocket (Figures 3A–3C).

In structures of full-length XKR8 and XKR9 (but not XKR4), C-terminal peptides occupy this pocket.[28–30,33] Unlike XKR1, XKR8 and XKR9 in cells are activated when caspases cleave their C termini to vacate the pocket, and thus the presence of the peptide in the pocket was speculated to be inhibitory,[28,29,33] although such inhibition has never been demonstrated in a reconstituted system.

To test the PH domain's effect on XKR1 scrambling, we carried out well-established *in vitro* scrambling assays[34] with FLAG-tagged XKR1 alone versus a FLAG-tagged XKR1-PH fusion construct, wherein the PH domain of VPS13A was fused to the XKR1 C terminus. In these assays, candidate scramblases are reconstituted into liposomes containing trace amounts of nitrobenzoxadiazole (NBD)-labeled lipids, and then a reducing agent (dithionite) is added. In liposomes lacking an active scramblase, dithionite reduces only NBD-lipids in the cytosol accessible leaflet of the liposome membrane, leading to a 50% reduction in NBD fluorescence. The reduction is larger when a scramblase is present to equilibrate NBD-lipids between the inner and outer leaflets, so that they are all dithionite accessible (Figure 3D). As shown before,[9] XKR1 by itself scrambles. Moreover, the XKR1-PH construct also scrambles, indicating that the binding of PH domain and insertion of PH-$L_{\beta6\text{-}\beta7}$ into XKR1's conserved cytosolic pocket do not abrogate XKR1 scrambling activity (Figure 3D). XKR1 therefore is active as a scramblase in the complex with VPS13A.

We propose that in XKR1 as well as in other XK-related proteins, the conserved surface pocket represents a binding site for protein partners, like VPS13A for XKR1. While activation of XKR8 and XKR9 *in cellulo* correlates with removal of their C-terminal peptides from the conserved surface pocket, the function of the C termini may not be inhibitory. For example, their removal in XKR8 and XKR9 might contribute to the recruitment of protein factors that collaborate with the XK-related proteins in their physiological function of apoptosis.

XKR1 scrambling mechanism

The best characterized scramblases, such as those in the TMEM16 family, feature a hydrophilic groove facing the greasy membrane core that allows lipid head groups to slide through the membrane, like a credit card through a reader.[35,36] We did not observe such a groove in the model of XKR1 derived from the cryo-EM reconstruction, nor has such a groove been identified in the experimentally derived structures of other XK-related proteins.[28–30]

As a first step to characterize the mechanism of lipid scrambling by XKR1, we performed all-atom MD (AA-MD) simulations of the cryo-EM-derived XKR1 structure embedded in a lipid bilayer, either alone as a monomer, in the presence of the PH domain of VPS13A, or in the presence of the entire C-terminal region of VPS13A that includes the PH domain (see Table S2 for a detailed description of the simulated systems). We observed that when bound to the PH domain of VPS13A, XKR1 spontaneously undergoes a conformational change with respect to the cryo-EM structure, characterized by a marked opening of the distance between TM1 and TM4 (Figures 3E–3G). Because several other scramblases have been recently proposed to be sensitive to membrane tension[37,38] and as we suspect that membrane tension could play a role in lipid dynamics via the VPS13A/XKR1 complex, as discussed further below (see discussion), we also tested the effect of increasing membrane tension in AA-MD simulations on XKR1's conformation. We found that increased membrane tension, which corresponds to allowing the bilayer to expand laterally, resulting in higher area per lipid, also favors a conformational transition in which TM1 and TM4 separate (Figures S3A–S3C). The opening between TM1 and TM4 is associated with an increased water permeation and the binding of one lipid at the cytosolic side of the interface between TM1 and TM4, likely priming the phospholipid for exposure to the extracellular leaflet (Figures 3H–3J).

Since no complete lipid translocations were observed in any of the AA-MD simulations, consistent with previous AA-MD simulations of XKR4,[30] we next performed enhanced sampling simulations to estimate the free energy barrier for lipid translocation along the aforementioned interface between TM1 and TM4 (Figure 3K). These calculations indicate that while the free energy barrier for lipid translocation in a protein-free system is ≈20 kcal/mol,[39] the barrier is significantly smaller (4 kcal/mol) when XKR1 is in the "open" conformation, supporting that the opening of the interface between TM1 and TM4 could lead to lipid scrambling.

To further test this hypothesis, we next converted the "closed" conformation observed in the cryo-EM reconstruction and the open conformation from AA-MD simulations to coarse grain (CG) resolution, and we assessed lipid scrambling using the MARTINI 3 force field,[40] an approach that was recently instrumental in the identification of multiple scramblases.[41–44] In support of our hypothesis, CG-MD simulations indicate that while the closed conformations for XK-related proteins observed by cryo-EM, including XKR1, XKR4, XKR8, and XKR9, are unable to scramble lipids, the open structure of XKR1 can (Figure 3L). The CG simulations confirm that the lipid scrambling pathway proceeds through a cavity between TM1 and TM4 lined with polar residues (Figure 3M).

Overall, our simulations indicate that while the structure of XKR1 emerging from the cryo-EM analysis represents a scrambling-inactive state, its activation when membrane embedded is likely to involve opening of a polar groove at the extracellular side of the interface between TM1 and TM4 helices, and this is likely to occur spontaneously when reconstituted in liposomes.

VPS13A binds and remodels membranes via its ATG2_C motif

Lipid extraction from donor membranes and insertion into acceptor membranes pose energetic barriers that must somehow be overcome for efficient BLTP-mediated bulk lipid transfer. Therefore, we next examined the interaction of the VPS13A-XKR1 complex with membranes to investigate whether the

Please cite this article in press as: Hu et al., Mechanism of lipid transfer by bridge-like protein VPS13A and the scramblase XK, Cell (2026), https://doi.org/10.1016/j.cell.2026.05.027

cryo-EM structure is compatible with lipid delivery and to identify factors that might facilitate lipid transport.

To investigate the interaction between the VPS13A-XKR1 complex and lipid membranes with high spatial resolution, we turned to CG-MD simulations of the entire complex embedded into a plasma membrane-like model lipid bilayer (see Table S3 for details on lipid composition). A challenge arising from the cryo-EM reconstruction is that some of the elements in VPS13A's C terminus that might mediate membrane association are disordered or highly mobile and could not be determined from the cryo-EM map. This is because the VPS13A sample in the cryo-EM reconstruction was not associated with membranes. Of particular interest among the disordered regions are the amphipathic helices of the ATG2_C motif, as they are known to play important roles in the localization of both VPS13 and ATG2 family BLTPs[4,15]; also, amphipathic helices have the ability to bind and remodel membranes,[45] which may play a role in lipid exchange.

After modeling the missing ATG2_C region back into the VPS13A structure (see STAR Methods), our simulations indicate that the architecture of the VPS13A-XKR1 complex is indeed compatible with direct interactions between VPS13A's bridge-domain and the cytosolic leaflet of the plasma membrane (Figures 4A and 4B). Specifically, while anchored to XKR1 via its PH domain, VPS13A binds to the membrane via its ATG2_C motif, which directly embeds into the bilayer with its amphipathic helices (Figure 4B). Notably, the ATG2_C motif does not adopt a single conformation with respect to either XKR1 or the rest of VPS13A, but it remains highly mobile even in its membrane-associated state (Figures 4C, 4D, S3D, and S3E).

Deletion of the ATG2_C motif (but not of the PH domain) from full-length VPS13A disrupts the interaction between the protein and the membrane in the CG-MD simulations, promoting dissociation of the VPS13A lipid-transport bridge from the bilayer (Figure 4B). To validate this observation, we next tested the role of VPS13A's ATG2_C motif in protein-membrane interactions by performing liposome flotation assays. These show that the ATG2_C motif supports membrane association of VPS13A (Figure 4E).

Further, our CG-MD simulations show that the presence of XKR1 causes significant remodeling of the surrounding membrane environment. First, consistent with observations for other scramblases, XKR1 promotes local membrane thinning (~15 Å) (close to helices IH1 and IH2; Figures 4F and S3F).[30,35] This distortion parallels observations from the cryo-EM reconstruction, where the detergent micelle surrounding XKR1 is asymmetric, with a ~25% thinning around XKR1 IH1 and IH2 (Figure 4G). Of note, this thinning is not proximal to the proposed site of lipid scrambling by XKR1 (i.e., the TM1–TM4 interface; Figure 3) but is rather close to where the VPS13A bridge-domain is expected to interact with the membrane. Moreover, the presence of XKR1 induces non-negligible membrane curvature in its surroundings (Figures 5A and S4A). This curvature is further enhanced by the ATG2_C motif of VPS13A (Figure S4A), indicating cooperation between the various components of the complex toward membrane remodeling, potentially to promote lipid transport by the VPS13A bridge-domain.

Direct lipid transfer from the VPS13A bridge-domain to the proximal membrane

In the CG-MD simulations of the membrane-bound structure of VPS13A (Figures 5A–5C and S4C), no spontaneous delivery of lipids to the proximal membrane was observed, even when the protein was fully bound to the lipid bilayer via its ATG2_C motif (as in Figures 4A and 4B). Rather, lipids inside the VPS13A cavity accumulated in proximity to the tube exit, but they remained at an average distance of 2 nm from the acceptor membrane (Figures 5A and 5B). Estimation of the free energy barrier required for such transfer by means of a potential of mean force (PMF) calculation using CG-MD simulations indicates a value of around 10 kcal/mol for the lipid transfer barrier when the protein is filled with 54 lipids (Figure S4B), a value that is consistent with the absence of spontaneous lipid delivery in the unbiased CG-MD simulations.

Since VPS13A-bound lipids tend to accumulate toward the protein extremity that is close to the membrane (Figure 5B), we next opted to increase the number of lipids inside the hydrophobic cavity of VPS13A, as a proxy to model lipid synthesis from the ER, and to subsequently perform unbiased CG-MD simulations of the complex in the presence of different lipid loads (ranging from 54 to 93 lipids; Table S3). Consistent with our previous observation, no delivery was observed when the total number of lipids in the entire VPS13A hydrophobic cavity was below 85 (Figure 5C). In contrast, we observed extensive lipid transfer (up to 27 lipids) in multiple unbiased simulations in the presence of a high lipid loads (Figures 5C, S4C, and S4D; Videos S1, S2, and S3; Table S3). In detail, the excess lipids start gathering near the C-terminal cap of the protein, with the head groups protruding out of the hydrophobic cavity and facing the membrane (Figure 5D, left). Simultaneously, and consistent with the 3D variability analysis from the cryo-EM data (Figure 2F), helices present in the cap (residues 2,799–2,810 and 2,839–2,860) were not conformationally restrained, allowing the opening of the lipid-transfer groove toward the membrane (Figure 5D, center). Eventually, the gathered lipids make contact with the membrane, and they are delivered in bulk (Figure 5D, right). In multiple replicates, lipid delivery occurs concomitantly with significant conformational transitions of both the cap helices, which start interacting with the membrane, and the ATG2_C motif (Figure 5D). Of note, the delivery process can be accelerated by increasing membrane tension in the acceptor bilayer (Figure 5C), which may lower the energy of lipid insertion into the membrane.

Finally, analogous simulations of lipid-loaded VPS13A in the presence of the open conformation of XKR1 (rather than in the experimentally observed closed conformation) confirm that while lipid delivery and lipid scrambling occur at the same time in the simulations, they remain spatially distinct (Figure 5E; Video S3). Lipids are delivered at a distance of ~7 nm from the lipid scramblase, which scrambles any lipid in its proximity and not only newly delivered ones (Figure 5E).

DISCUSSION

Together, our experimental structure of the VPS13A/CaM-XKR1 complex and MD analysis suggest that lipid delivery is activated when VPS13A interfaces with its binding partner XKR1 in the

Please cite this article in press as: Hu et al., Mechanism of lipid transfer by bridge-like protein VPS13A and the scramblase XK, Cell (2026), https://doi.org/10.1016/j.cell.2026.05.027

CellPress
OPEN ACCESS

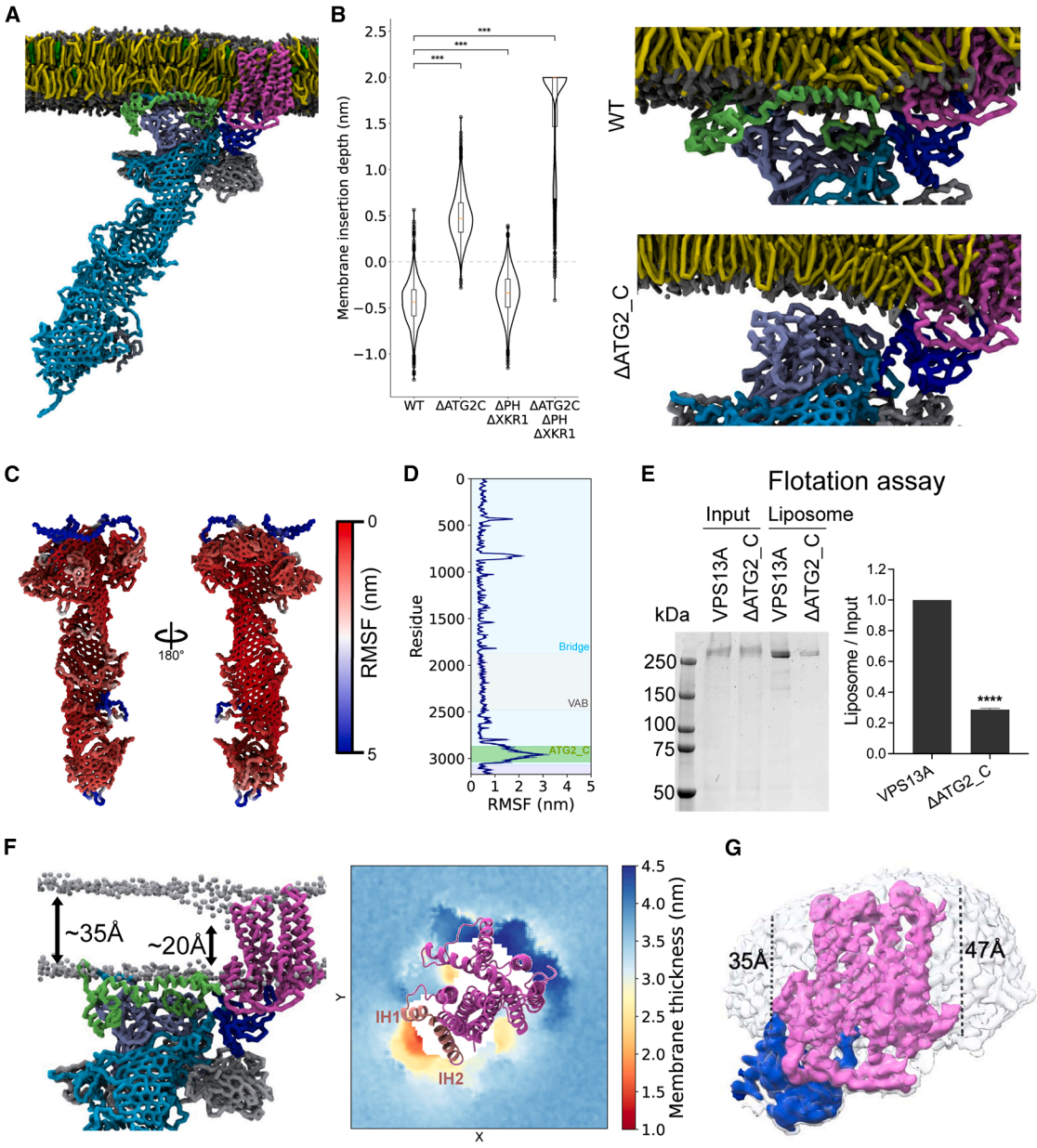

Figure 4. The membrane interaction of the VPS13A-XKR1 complex is mediated by its ATG2_C domain

(A) Snapshot of the CG model of VPS13A/CaM-XKR1 complex embedded in a plasma membrane-like membrane; the color scheme of the different domains and monomers matches that used in Figure 1.

(B) Insertion depth (in nm) of wild-type VPS13A and mutants into the membrane, computed as the difference between protein's z coordinate and the local z coordinate of the bilayer head groups. Representative snapshots (right) show the membrane interface between of wild-type VPS13A and of the ΔATG2_C mutant. Statistical analysis was performed using ordinary one-way ANOVA and Welch's pairwise comparisons with Bonferroni correction (***$p < 0.001$, $n = 3$ replicates).

(C) 3D view of the VPS13A structure colored according to the root mean square fluctuation (RMSF) values in the CG-MD simulations. Colors range from red (low flexibility) to dark blue (high flexibility). $n = 3$ replicates.

(D) RMSF values for the CG-MD simulations shown in (C). $n = 3$ replicates.

(E) Membrane association of full-length VPS13A and ΔATG2_C mutant analyzed by biochemical flotation assay. A representative SDS-PAGE gel shows reduced flotation of ΔATG2_C mutant with liposomes, compared with wild-type VPS13A. Quantification from three independent experiments is shown in the right. Data are presented as mean ± SD. Statistical analysis was performed using an unpaired Welch's t test (****$p < 0.0001$) in GraphPad Prism.

(F) Snapshot and membrane thickness xy map from CG-MD simulations showing local membrane thinning around helices IH1 and IH2 of XKR1.

(G) Cryo-EM density of XKR1-PH complex, with XKR1 embedded in GDN detergent micelles visualized as a transparent white density. The micelle thickness was measured at two opposing sides surrounding XKR1 in ChimeraX.

See also Figures S3 and S4.

Please cite this article in press as: Hu et al., Mechanism of lipid transfer by bridge-like protein VPS13A and the scramblase XK, Cell (2026), https://doi.org/10.1016/j.cell.2026.05.027

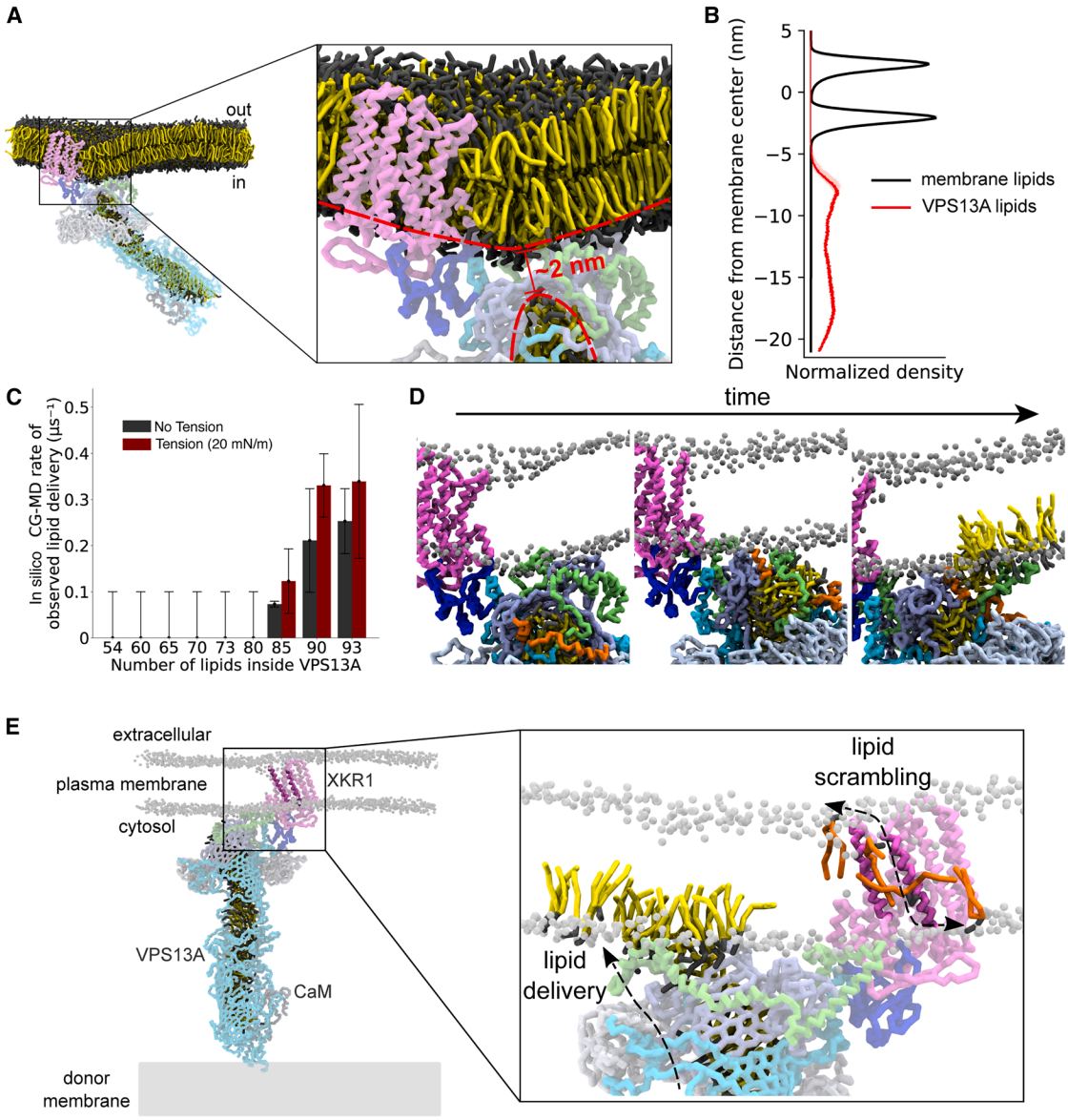

Figure 5. The VPS13A-XKR1 complex is compatible with bulk lipid delivery

(A) Snapshot of the lipid-filled VPS13A-XKR1 complex. The inset highlights both the local membrane curvature induced by the complex and the distance between the lipids inside the bridge-domain from the lipid bilayer. The protein is colored as in Figure 1A.

(B) Density profile of phosphate groups for lipids in the bilayer (black line) and from those inside the bridge-domain from VPS13A (red line).

(C) Rate of lipid delivery from VPS13A to the lipid bilayer as a function of the number of lipids inside the bridge-domain of VPS13A. The boxes and error bars represent the mean and standard deviation, respectively. $n = 3$ for each condition. The black boxes correspond to simulations with no membrane tension and the red boxes to simulations with membrane tension of 20 mN/m.

(D) Representative snapshots from CG-MD simulations describing bulk lipid delivery from the VPS13A hydrophobic groove (loaded with 93 lipids) to the lipid bilayer. Delivered lipids are colored in yellow, phosphate groups of the membrane lipids are displayed as gray spheres, the protein is colored as in (A).

(E) Schematic model describing the spatial separation between the two main functions of the VPS13A/CaM-XKR1 complex: lipid delivery and lipid scrambling. Lipids delivered are shown in yellow sticks. Lipid scrambling is shown by overlapping multiple MD snapshots of a lipid scrambling along the interface between TM1 and TM4 of XKR1.

See also Figure S4.

acceptor membrane, and then lipids are delivered directly from the bridge-domain of VPS13A to the cytosolic leaflet of the plasma membrane. The interaction between VPS13A's PH domain and XKR1, conformational changes in VPS13A's C-terminal cap and its VAB domain, and membrane insertion of the amphipathic helices of VPS13A's ATG2_C motif are required to juxtapose the end of the bridge-domain to the proximal membrane, so that lipids can move from the hydrophobic

Please cite this article in press as: Hu et al., Mechanism of lipid transfer by bridge-like protein VPS13A and the scramblase XK, Cell (2026), https://doi.org/10.1016/j.cell.2026.05.027

environment within the bridge to the membrane without desolvation of their acyl chains. Our studies suggest that the VPS13A-XKR1 complex introduces significant local membrane deformations in the acceptor membrane where lipid transfer from the VPS13A bridge is expected to take place. These deformations impact lipid packing and may lower the energy barrier for lipid insertion into the acceptor membrane.[46]

Importantly, we were able to observe robust lipid transfer *in silico* when lipids were present in excess inside the bridge-domain, a condition that mimics lipid synthesis at the ER. Further, lipid release was accelerated by an increase in membrane tension at the acceptor membrane. These results support current thinking that directional BLTP-mediated lipid flow could be driven by differences in membrane tension between donor and acceptor membranes.[1,47] The ER, the donor membrane where most structural lipids are synthesized, has low membrane tension, whereas membrane tension in other cellular organelles is higher.[48] How the differences in membrane tension arise is not currently well understood and is a topic attracting significant attention.[49]

VPS13A delivers its lipids to the cytosolic leaflet of the membrane close to XKR1, which can then equilibrate newly delivered lipids between leaflets of the bilayer. As assessed *in silico*, the XKR1 conformation observed in the cryo-EM reconstruction does not support lipid scrambling, nor do experimental structures for other XK family members.[30,42] AA-MD simulations for XKR1 suggest, however, that another conformation exists, where TM1 and TM4 have moved apart to form a polar channel through which lipids can slide between bilayer leaflets. Both XKR1 and an XKR1-PH fusion construct scrambled lipids when embedded in liposomes *in vitro*, supporting that XKR1 may adopt a scrambling active conformation in membranes versus in a detergent micelle as in the cryo-EM reconstruction. This observation parallels observations for TMEM16 scramblases at the plasma membrane, which also undergo opening/closing of their hydrophilic grooves to regulate lipid scrambling activity.[50–52] Mutational analyses of XKR4 and XKR8[29,30] are consistent with the proposal that a polar groove between TM1 and TM4 opens to enable scrambling, but whether the remaining members of the XK-related family (XKR2, XKR3, XKR5-7, and XKR9) act by the same mechanism remains to be investigated.

We find it intriguing that *in silico* simulations indicate that higher membrane tension both accelerates lipid delivery by VPS13A (Figure 5C) and promotes XKR1's open, lipid-scrambling-competent conformation (Figure S3C). Together, these observations suggest that although there is no direct physical connection between VPS13A's bridge-domain and XKR1, lipid delivery by the BLTP and the scramblase might nevertheless be coupled by physical or chemical modifications of bilayer properties.

In the VPS13A-XKR1 complex under study here, its PH domain plays a primary role in targeting VPS13A to XKR1 at the plasma membrane, where it coordinates with the ATG2_C motif in firmly anchoring the bridge-domain to the membrane. We cannot exclude that the VAB and WWE domains may assist in membrane binding via additional interactions. Moreover, VPS13A also functions at other cellular locations[15] together with receptors other than XKR1, where the VAB or WWE domains or some combination of the PH, VAB, and WWE domains could mediate organelle attachment. We envision that the VAB or WWE domains could have the same function as the PH domain in positioning the bridge-domain with respect to the acceptor membrane. The VPS13 proteins, including VPS13B, VPS13C, and VPS13D, in humans as well as those in other organisms share a similar architecture, with shared built-in adaptor modules (ATG2_C, PH, VAB; the WWE domain is present only in VPS13A and VPS13C). Thus, the structure of the VPS13A/CaM-XKR1 complex we describe here is applicable to understand lipid delivery by all VPS13 proteins.

The ATG2 proteins, which are related to the VPS13s, lack most of the built-in adaptor domains of the VPS13 family, and instead they rely on exogenous partner proteins for their localization. They are streamlined versions of VPS13, pared down to the bridge-domain and the ATG2_C amphipathic helices. ATG2 cooperates with the scramblase ATG9 during autophagy and can bind to it directly.[8,53] Based on our current study of VPS13A lipid delivery, we propose that lipids are transferred from the bridge-domain of ATG2 directly to membrane, where the ATG2_C motif and the ATG2-ATG9 interaction appose the bridge-domain close to the acceptor membrane while also localizing the BLTP near a scramblase. Recent MD studies support that ATG2 could deliver lipid directly to the acceptor membrane and describe a role for the ATG2_C amphipathic helices in membrane deformation during this process.[54] Notably, in cells during autophagy, ATG9 localizes to the rim of the nascent autophagosome,[55] which is highly curved.

In contrast to our model, earlier studies of the ATG2-ATG9 complex at low resolution had led to speculation that ATG2 delivers lipids to the scramblase rather than directly to the membrane and that the scramblase then integrates the lipids into the membrane.[24,53] Another interpretation of the earlier data is consistent with the model put forth here, i.e., that ATG2 is tethered to ATG9 to bring it to the membrane in the proximity of scrambling activity, even as lipids are transferred from the bridge-domain directly to the membrane. Thus, our study significantly advances our understanding of lipid delivery by BLTPs in the ATG2 family. Other less studied BLTP families, whose members also lack the ATG2_C amphipathic helices, could also deliver lipids directly to the acceptor membrane, although the features responsible for membrane binding and deformation remain to be identified.

A recent atomic resolution study of a BLTP1-containing complex that forms at the donor membrane (ER) showed that lipids likely enter the BLTP1 bridge-domain via an integral membrane protein vestibule, consisting of five TM helices.[25,43] Our study here complements the BLTP1 study insofar as we describe mechanisms for lipid transfer out of the bridge-domain and back into the membrane. Arguably unexpectedly, the lipid transfer process at the acceptor membrane—where, at least for the VPS13s, lipids are transferred directly to the membrane—does not mirror the extraction process at the donor membrane observed for BLTP1. We look forward to further studies on BLTP proteins and processes at both ends, which should help with understanding how general each of these strategies is.

Limitations of the study

In the cryo-EM study, XKR1 was solubilized in a detergent micelle, rather than embedded in the membrane. Thus, although the structure shows that the bridge-domain's C-terminal end of VPS13A is positioned to interact directly with the acceptor membrane, where

the plane of the membrane is extrapolated based on the XKR1 structure, the cryo-EM data do not directly show the interaction between VPS13A and the membrane. Namely, it is unclear from the experimental structure whether accessory domains like the VAB, WWE, or PH domains might interact with the membrane and, importantly regarding the lipid transfer process, how the C-terminal cap and the amphipathic helices of the ATG2_C motif are arranged with respect to the lipid bilayer. In the absence of an experimental structure visualizing the interaction, we have relied on MD simulations to better understand how the complex interfaces with the membrane to deliver lipids.

MD simulations have intrinsic limitations to their accuracy (which depend on the force field used, either at AA or CG resolution) and sampling, which in this case is alleviated by performing multiple microsecond-long individual replicates. For CG simulations, this might result in accelerated processes and unphysical rates, such as those measured for both scrambling and lipid delivery (Figures 3L and 5C). For the CG simulations, one additional limitation is the use of an elastic network to maintain the secondary structures found in the cryo-EM structure. However, no elastic network was used for unstructured or disordered domains, such as the ATG2_C motif, that were free to sample their conformational space according to the force field energy landscape.

When applied to the cryo-EM structures, the MD simulations support that the direct transfer of lipids between the bridge-domain and the membrane is plausible, particularly in the presence of a "driving force," for example, lipid biosynthesis in the donor membrane. A limitation to testing the *in silico* predictions in a reconstituted system is that a physiologically relevant *in vitro* assay has not yet been developed. While we and others have shown that BLTPs can transfer lipids between liposomes,[15,27] the BLTPs most likely act as shuttles between the liposomes in these *in vitro* systems; and thus far, the field has not reconstituted a system in which the BLTPs are demonstrated to act as channels through which lipids flow directionally. There are two major hurdles to overcome. First, the proteins that mediate association between VPS13s and the donor membrane, usually the ER, are only incompletely identified, so it is unclear how to attach VPS13 to the donor membrane in a physiologically relevant manner. And second, we have not yet developed protocols to recapitulate increased membrane tension, as might result from lipid biosynthesis in just the outer leaflet in the donor liposomes. We look forward to the development of such assays, which will be key in assessing the nature of the driving force.

RESOURCE AVAILABILITY

Lead contact

Further information and requests for resources and reagents should be directed to and will be fulfilled by the lead contact, Karin Reinisch (karin.reinisch@yale.edu).

Materials availability

Plasmids generated in this study are available upon request to the lead contact.

Data and code availability

Cryo-EM maps are deposited in the EMDB (EMDB: EMD-72912, EMD-72909, and EMD-72913), and coordinates derived from each of the maps are deposited in the PDB (PDB: 9YG4, 9YFW, and 9YG5). Input files for all MD trajectories are deposited in Zenodo: https://doi.org/10.5281/zenodo.19002741.

ACKNOWLEDGMENTS

We thank Drs. J. Lees and A. Accardi for discussions regarding cryo-EM data processing and XKR protein scrambling mechanisms, respectively, and H. Zhou and S. Hamill for technical assistance. This work was funded by the NIH (grants R35GM131715 to K.M.R. and DA018343 to P.D.C.), the Swiss National Science Foundation (grant CR00I5-236020 to S.V.), and the European Research Council under the European Union's Horizon 2020 research and innovation program (grant agreement no. 803952 to S.V.). This work was supported by grants from the Swiss National Supercomputing Centre under project IDs s1269, lp24, and lp69. D.Á. acknowledges support from the Margarita Salas program 2021–2023 funded by Ministerio de Universidades (MU-21-UP2021-030-53773022).

AUTHOR CONTRIBUTIONS

K.M.R., B.H., D.Á., C.R.-R., and S.V. conceived and supervised this project. B.H. carried out the cryo-EM analysis of the VPS13A/CaM-XKR1 complex and biochemical experiments; C.R.-R. investigated XKR1 scrambling activity *in silico*; V.G. determined the effect of the complex on membranes *in silico*; D.Á. performed *in silico* investigation of lipid transfer together with Y.A. D.L. modeled the VPS13A N terminus and its interaction with CaM and shared his coordinates for the lipid-transfer inactive VPS13C complex before publication. X.W. and P.D.C. shared unpublished data regarding the interaction between VPS13A's ATG2_C motif and membranes and were invaluable in discussions. K.M.R. and S.V. wrote the manuscript, with input from all authors.

DECLARATION OF INTERESTS

The authors declare no competing interests.

STAR★METHODS

Detailed methods are provided in the online version of this paper and include the following:

- KEY RESOURCES TABLE
- EXPERIMENTAL MODEL AND STUDY PARTICIPANT DETAILS
  - Bacterial strain
  - Cell lines
- METHOD DETAILS
  - Protein expression and purification
  - Cryo-EM sample preparation and data collection
  - Image processing
  - Model refinement and validation
  - Liposome preparation and flotation assay
  - Scrambling assay
  - System setup and simulation details
  - MD simulations analysis
- QUANTIFICATION AND STATISTICAL ANALYSIS

SUPPLEMENTAL INFORMATION

Supplemental information can be found online at https://doi.org/10.1016/j.cell.2026.05.027.

Received: September 28, 2025
Revised: March 14, 2026
Accepted: May 18, 2026

REFERENCES

1. Reinisch, K.M., De Camilli, P., and Melia, T.J. (2025). Lipid Dynamics at Membrane Contact Sites. Annu. Rev. Biochem. *94*, 479–502. https://doi.org/10.1146/annurev-biochem-083024-122821.

2. Melia, T.J. (2023). Growing thin - How bulk lipid transport drives expansion of the autophagosome membrane but not of its lumen. Curr. Opin. Cell Biol. *83*, 102190. https://doi.org/10.1016/j.ceb.2023.102190.

3. Reinisch, K.M., and Prinz, W.A. (2021). Mechanisms of nonvesicular lipid transport. J. Cell Biol. *220*, e202012058. https://doi.org/10.1083/jcb.202012058.

4. Wang, X., Xu, P., Bentley-DeSousa, A., Hancock-Cerutti, W., Cai, S., Johnson, B.T., Tonelli, F., Shao, L., Talaia, G., Alessi, D.R., et al. (2025). The bridge-like lipid transport protein VPS13C/PARK23 mediates ER-lysosome contacts following lysosome damage. Nat. Cell Biol. *27*, 776–789. https://doi.org/10.1038/s41556-025-01653-6.

5. Hanna, M., Guillén-Samander, A., and De Camilli, P. (2023). RBG Motif Bridge-Like Lipid Transport Proteins: Structure, Functions, and Open Questions. Annu. Rev. Cell Dev. Biol. *39*, 409–434. https://doi.org/10.1146/annurev-cellbio-120420-014634.

6. Matoba, K., Kotani, T., Tsutsumi, A., Tsuji, T., Mori, T., Noshiro, D., Sugita, Y., Nomura, N., Iwata, S., Ohsumi, Y., et al. (2020). Atg9 is a lipid scramblase that mediates autophagosomal membrane expansion. Nat. Struct. Mol. Biol. *27*, 1185–1193. https://doi.org/10.1038/s41594-020-00518-w.

7. Maeda, S., Yamamoto, H., Kinch, L.N., Garza, C.M., Takahashi, S., Otomo, C., Grishin, N.V., Forli, S., Mizushima, N., and Otomo, T. (2020). Structure, lipid scrambling activity and role in autophagosome formation of ATG9A. Nat. Struct. Mol. Biol. *27*, 1194–1201. https://doi.org/10.1038/s41594-020-00520-2.

8. Ghanbarpour, A., Valverde, D.P., Melia, T.J., and Reinisch, K.M. (2021). A model for a partnership of lipid transfer proteins and scramblases in membrane expansion and organelle biogenesis. Proc. Natl. Acad. Sci. USA *118*, e2101562118. https://doi.org/10.1073/pnas.2101562118.

9. Adlakha, J., Hong, Z., Li, P., and Reinisch, K.M. (2022). Structural and biochemical insights into lipid transport by VPS13 proteins. J. Cell Biol. *221*, e202202030. https://doi.org/10.1083/jcb.202202030.

10. Rampoldi, L., Dobson-Stone, C., Rubio, J.P., Danek, A., Chalmers, R.M., Wood, N.W., Verellen, C., Ferrer, X., Malandrini, A., Fabrizi, G.M., et al. (2001). A conserved sorting-associated protein is mutant in chorea-acanthocytosis. Nat. Genet. *28*, 119–120. https://doi.org/10.1038/88821.

11. Ho, M., Chelly, J., Carter, N., Danek, A., Crocker, P., and Monaco, A.P. (1994). Isolation of the gene for McLeod syndrome that encodes a novel membrane transport protein. Cell *77*, 869–880. https://doi.org/10.1016/0092-8674(94)90136-8.

12. Park, J.S., and Neiman, A.M. (2020). XK is a partner for VPS13A: a molecular link between Chorea-Acanthocytosis and McLeod Syndrome. Mol. Biol. Cell *31*, 2425–2436. https://doi.org/10.1091/mbc.E19-08-0439-T.

13. Ryoden, Y., Segawa, K., and Nagata, S. (2022). Requirement of Xk and Vps13a for the P2X7-mediated phospholipid scrambling and cell lysis in mouse T cells. Proc. Natl. Acad. Sci. USA *119*, e2119286119. https://doi.org/10.1073/pnas.2119286119.

14. Guillén-Samander, A., Wu, Y., Pineda, S.S., García, F.J., Eisen, J.N., Leonzino, M., Ugur, B., Kellis, M., Heiman, M., and De Camilli, P. (2022). A partnership between the lipid scramblase XK and the lipid transfer protein VPS13A at the plasma membrane. Proc. Natl. Acad. Sci. USA *119*, e2205425119. https://doi.org/10.1073/pnas.2205425119.

15. Kumar, N., Leonzino, M., Hancock-Cerutti, W., Horenkamp, F.A., Li, P., Lees, J.A., Wheeler, H., Reinisch, K.M., and De Camilli, P. (2018). VPS13A and VPS13C are lipid transport proteins differentially localized at ER contact sites. J. Cell Biol. *217*, 3625–3639. https://doi.org/10.1083/jcb.201807019.

16. Li, D., Wang, X., Hu, B., Hao, H., Hamill, S., Li, Y., Chen, G., De Camilli, P., and Reinisch, K.M. (2025). Insights into the regulation of VPS13 family bridge-like lipid transfer proteins from the structure of VPS13C. Preprint at bioRxiv. https://doi.org/10.1101/2025.11.10.687702.

17. Levine, T.P. (2022). Sequence Analysis and Structural Predictions of Lipid Transfer Bridges in the Repeating Beta Groove (RBG) Superfamily Reveal Past and Present Domain Variations Affecting Form, Function and Interactions of VPS13, ATG2, SHIP164, Hobbit and Tweek. Contact *5*, 251525642211343. https://doi.org/10.1177/25152564221134328.

18. Jumper, J., Evans, R., Pritzel, A., Green, T., Figurnov, M., Ronneberger, O., Tunyasuvunakool, K., Bates, R., Žídek, A., Potapenko, A., et al. (2021). Highly accurate protein structure prediction with AlphaFold. Nature *596*, 583–589. https://doi.org/10.1038/s41586-021-03819-2.

19. Emsley, P., Lohkamp, B., Scott, W.G., and Cowtan, K. (2010). Features and development of Coot. Acta Crystallogr. D Biol. Crystallogr. *66*, 486–501. https://doi.org/10.1107/S0907444910007493.

20. Meng, E.C., Goddard, T.D., Pettersen, E.F., Couch, G.S., Pearson, Z.J., Morris, J.H., and Ferrin, T.E. (2023). UCSF ChimeraX: Tools for structure building and analysis. Protein Sci. *32*, e4792. https://doi.org/10.1002/pro.4792.

21. Terashi, G., Wang, X., Prasad, D., Nakamura, T., and Kihara, D. (2024). DeepMainmast: integrated protocol of protein structure modeling for cryo-EM with deep learning and structure prediction. Nat. Methods *21*, 122–131. https://doi.org/10.1038/s41592-023-02099-0.

22. Liebschner, D., Afonine, P.V., Baker, M.L., Bunkóczi, G., Chen, V.B., Croll, T.I., Hintze, B., Hung, L.W., Jain, S., McCoy, A.J., et al. (2019). Macromolecular structure determination using X-rays, neutrons and electrons: recent developments in Phenix. Acta Crystallogr. D Struct. Biol. *75*, 861–877. https://doi.org/10.1107/S2059798319011471.

23. Li, P., Lees, J.A., Lusk, C.P., and Reinisch, K.M. (2020). Cryo-EM reconstruction of a VPS13 fragment reveals a long groove to channel lipids between membranes. J. Cell Biol. *219*, e202001161. https://doi.org/10.1083/jcb.202001161.

24. Wang, Y., Dahmane, S., Ti, R., Mai, X., Zhu, L., Carlson, L.A., and Stjepanovic, G. (2024). Structural basis for lipid transfer by the ATG2A-ATG9A complex. Nat. Struct. Mol. Biol. *32*, 35–47. https://doi.org/10.1038/s41594-024-01376-6.

25. Kang, Y., Lehmann, K.S., Long, H., Jefferson, A., Purice, M., Freeman, M., and Clark, S. (2025). Structural basis of lipid transfer by a bridge-like lipid-transfer protein. Nature *642*, 242–249. https://doi.org/10.1038/s41586-025-08918-y.

26. Srinivasan, S., Álvarez, D., John Peter, A.T., and Vanni, S. (2024). Unbiased MD simulations identify lipid binding sites in lipid transfer proteins. J. Cell Biol. *223*, e202312055. https://doi.org/10.1083/jcb.202312055.

27. Valverde, D.P., Yu, S., Boggavarapu, V., Kumar, N., Lees, J.A., Walz, T., Reinisch, K.M., and Melia, T.J. (2019). ATG2 transports lipids to promote autophagosome biogenesis. J. Cell Biol. *218*, 1787–1798. https://doi.org/10.1083/jcb.201811139.

28. Straub, M.S., Alvadia, C., Sawicka, M., and Dutzler, R. (2021). Cryo-EM structures of the caspase-activated protein XKR9 involved in apoptotic lipid scrambling. eLife *10*, e69800. https://doi.org/10.7554/eLife.69800.

29. Sakuragi, T., Kanai, R., Tsutsumi, A., Narita, H., Onishi, E., Nishino, K., Miyazaki, T., Baba, T., Kosako, H., Nakagawa, A., et al. (2021). The tertiary structure of the human Xkr8-Basigin complex that scrambles phospholipids at plasma membranes. Nat. Struct. Mol. Biol. *28*, 825–834. https://doi.org/10.1038/s41594-021-00665-8.

30. Chakraborty, S., Feng, Z., Lee, S., Alvarenga, O.E., Panda, A., Zhang, S., Bruni, R., Khelashvili, G., Gupta, K., and Accardi, A. (2025). Structure and function of the human apoptotic scramblase Xkr4. Nat. Commun. *16*, 7317. https://doi.org/10.1038/s41467-025-62739-1.

31. Bartoš, L., Menon, A.K., and Vácha, R. (2024). Insertases scramble lipids: Molecular simulations of MTCH2. Structure *32*, 505–510. https://doi.org/10.1016/j.str.2024.01.012.

32. Park, J.S., Hu, Y., Hollingsworth, N.M., Miltenberger-Miltenyi, G., and Neiman, A.M. (2022). Interaction between VPS13A and the XK scramblase is important for VPS13A function in humans. J. Cell Sci. *135*, jcs260227. https://doi.org/10.1242/jcs.260227.

33. Sakuragi, T., Kanai, R., Otani, M., Kikkawa, M., Toyoshima, C., and Nagata, S. (2024). The role of the C-terminal tail region as a plug to regulate

XKR8 lipid scramblase. J. Biol. Chem. *300*, 105755. https://doi.org/10.1016/j.jbc.2024.105755.

34. Ploier, B., and Menon, A.K. (2016). A Fluorescence-based Assay of Phospholipid Scramblase Activity. J. Vis. Exp. https://doi.org/10.3791/54635.
35. Sebinelli, H.G., Syska, C., Čopič, A., and Lenoir, G. (2024). Established and emerging players in phospholipid scrambling: A structural perspective. Biochimie *227*, 111–122. https://doi.org/10.1016/j.biochi.2024.09.008.
36. Pomorski, T., and Menon, A.K. (2006). Lipid flippases and their biological functions. Cell. Mol. Life Sci. *63*, 2908–2921. https://doi.org/10.1007/s00018-006-6167-7.
37. Lee, H., Park, Y.C., Wen, H., Smith, H.E., Balaraman, J., Cui, R., Sotomayor, M., and Ballesteros, A. (2025). TMC1 and TMC2 are cholesterol-dependent scramblases that regulate membrane homeostasis in auditory hair cells. Preprint at bioRxiv. https://doi.org/10.1101/2025.07.03.663083.
38. Miyata, Y., Takahashi, K., Lee, Y., Sultan, C.S., Kuribayashi, R., Takahashi, M., Hata, K., Bamba, T., Izumi, Y., Liu, K., et al. (2025). Membrane structure-responsive lipid scrambling by TMEM63B to control plasma membrane lipid distribution. Nat. Struct. Mol. Biol. *32*, 185–198. https://doi.org/10.1038/s41594-024-01411-6.
39. Kroutil, O., Bartoš, L., Kabelka, I., and Vácha, R. (2025). Martini 3 Limitations in Phospholipid Flip-Flop. J. Chem. Theory Comput. *21*, 9227–9233. https://doi.org/10.1021/acs.jctc.5c00994.
40. Souza, P.C.T., Alessandri, R., Barnoud, J., Thallmair, S., Faustino, I., Grünewald, F., Patmanidis, I., Abdizadeh, H., Bruininks, B.M.H., Wassenaar, T.A., et al. (2021). Martini 3: a general purpose force field for coarse-grained molecular dynamics. Nat. Methods *18*, 382–388. https://doi.org/10.1038/s41592-021-01098-3.
41. Jahn, H., Bartoš, L., Dearden, G.I., Dittman, J.S., Holthuis, J.C.M., Vácha, R., and Menon, A.K. (2023). Phospholipids are imported into mitochondria by VDAC, a dimeric beta barrel scramblase. Nat. Commun. *14*, 8115. https://doi.org/10.1038/s41467-023-43570-y.
42. Li, D., Rocha-Roa, C., Schilling, M.A., Reinisch, K.M., and Vanni, S. (2024). Lipid scrambling is a general feature of protein insertases. Proc. Natl. Acad. Sci. USA *121*, e2319476121. https://doi.org/10.1073/pnas.2319476121.
43. Rocha-Roa, C., Chandran Blair, P., Sidhu, G., Álvarez, D., Davey, M., Conibear, E., and Vanni, S. (2026). TMEM170 proteins are lipid scramblases associated with bridge-type lipid transporters BLTP1/Csf1. Nat. Struct. Mol. Biol. *33*, 215–219. https://doi.org/10.1038/s41594-025-01716-0.
44. Javanainen, M., Šimek, J., Tranter, D., O'Keefe, S., Karki, S., Biriukov, D., Šachl, R., and Paavilainen, V.O. (2025). Lipid Scrambling Pathways in the Sec61 Translocon Complex. J. Am. Chem. Soc. *147*, 15970–15984. https://doi.org/10.1021/jacs.4c11142.
45. Giménez-Andrés, M., Čopič, A., and Antonny, B. (2018). The Many Faces of Amphipathic Helices. Biomolecules *8*, 45. https://doi.org/10.3390/biom8030045.
46. Álvarez, D., Blair, P.C., Rocha-Roa, C., Davey, M., Conibear, E., and Vanni, S. (2026). The molecular mechanism of lipid uptake by membrane-anchored bridge-like lipid transfer proteins. Proc. Natl. Acad. Sci. U S A. *123*, e2520399123. https://doi.org/10.1073/pnas.2520399123.
47. Zhang, Y., and Lin, C. (2024). Lipid osmosis, membrane tension, and other mechanochemical driving forces of lipid flow. Curr. Opin. Cell Biol. *88*, 102377. https://doi.org/10.1016/j.ceb.2024.102377.
48. Wang, H.Y., Rumin, A., Doktorova, M., Sputay, D., Chan, S.H., Wehman, A.M., Levental, K.R., and Levental, I. (2025). Loss of lipid asymmetry facilitates plasma membrane blebbing by decreasing membrane lipid packing. Proc. Natl. Acad. Sci. USA *122*, e2417145122. https://doi.org/10.1073/pnas.2417145122.
49. Barahtjan, P., Cook, K.C., Bočan, V., Lennartz, H.M., Jumel, T., Schuhmann, K., Traikov, S., Böhlig, K., Kuhn, S.M., López, C.J., et al. (2025). Disruption of Plasma Membrane Lipid Asymmetry Alters Cellular Energetics. Preprint at bioRxiv. https://doi.org/10.1101/2025.04.27.650841.
50. Khelashvili, G., Kots, E., Cheng, X., Levine, M.V., and Weinstein, H. (2022). The allosteric mechanism leading to an open-groove lipid conductive state of the TMEM16F scramblase. Commun. Biol. *5*, 990. https://doi.org/10.1038/s42003-022-03930-8.
51. Feng, Z., Alvarenga, O.E., and Accardi, A. (2024). Structural basis of closed groove scrambling by a TMEM16 protein. Nat. Struct. Mol. Biol. *31*, 1468–1481. https://doi.org/10.1038/s41594-024-01284-9.
52. Stephens, C.A., van Hilten, N., Zheng, L., and Grabe, M. (2025). Simulation-based survey of TMEM16 family reveals that robust lipid scrambling requires an open groove. eLife *14*, e105111. https://doi.org/10.7544/eLife.105111.
53. van Vliet, A.R., Chiduza, G.N., Maslen, S.L., Pye, V.E., Joshi, D., De Tito, S., Jefferies, H.B.J., Christodoulou, E., Roustan, C., Punch, E., et al. (2022). ATG9A and ATG2A form a heteromeric complex essential for autophagosome formation. Mol. Cell *82*, 4324–4339. https://doi.org/10.1016/j.molcel.2022.10.017.
54. Sakai, Y., Matoba, K., Kotani, T., Hao, L., Suzuki, K., Kakuta, C., Sugita, Y., Osawa, T., Nakatogawa, H., and Noda, N.N. (2025). Mechanism of bridge-type phospholipid transfer by Atg2 for autophagosome biogenesis. Preprint at bioRxiv. https://doi.org/10.1101/2025.05.24.655882.
55. Melia, T.J., Lystad, A.H., and Simonsen, A. (2020). Autophagosome biogenesis: From membrane growth to closure. J. Cell Biol. *219*, e202002085. https://doi.org/10.1083/jcb.202002085.
56. Abramson, J., Adler, J., Dunger, J., Evans, R., Green, T., Pritzel, A., Ronneberger, O., Willmore, L., Ballard, A.J., Bambrick, J., et al. (2024). Accurate structure prediction of biomolecular interactions with AlphaFold 3. Nature *630*, 493–500. https://doi.org/10.1038/s41586-024-07487-w.
57. Schindelin, J., Arganda-Carreras, I., Frise, E., Kaynig, V., Longair, M., Pietzsch, T., Preibisch, S., Rueden, C., Saalfeld, S., Schmid, B., et al. (2012). Fiji: an open-source platform for biological-image analysis. Nat. Methods *9*, 676–682. https://doi.org/10.1038/nmeth.2019.
58. Punjani, A., Rubinstein, J.L., Fleet, D.J., and Brubaker, M.A. (2017). cryoSPARC: algorithms for rapid unsupervised cryo-EM structure determination. Nat. Methods *14*, 290–296. https://doi.org/10.1038/nmeth.4169.
59. Abraham, M.J., Murtola, T., Schulz, R., Páll, S., Smith, J.C., Hess, B., and Lindahl, E. (2015). GROMACS: High performance molecular simulations through multi-level parallelism from laptops to supercomputers. SoftwareX *1–2*, 19–25. https://doi.org/10.1016/j.softx.2015.06.001.
60. Humphrey, W., Dalke, A., and Schulten, K. (1996). VMD: visual molecular dynamics. J. Mol. Graph. *14*, 33–38. https://doi.org/10.1016/0263-7855(96)00018-5.
61. Casañal, A., Lohkamp, B., and Emsley, P. (2020). Current developments in Coot for macromolecular model building of Electron Cryo-microscopy and Crystallographic Data. Protein Sci. *29*, 1055–1064. https://doi.org/10.1002/pro.3791.
62. Goddard, T.D., Huang, C.C., Meng, E.C., Pettersen, E.F., Couch, G.S., Morris, J.H., and Ferrin, T.E. (2018). UCSF ChimeraX: Meeting modern challenges in visualization and analysis. Protein Sci. *27*, 14–25. https://doi.org/10.1002/pro.3235.
63. Webb, B., and Sali, A. (2021). Protein Structure Modeling with MODELLER. Methods Mol. Biol. *2199*, 239–255. https://doi.org/10.1007/978-1-0716-0892-0_14.
64. Huang, J., Rauscher, S., Nawrocki, G., Ran, T., Feig, M., de Groot, B.L., Grubmüller, H., and MacKerell, A.D., Jr. (2017). CHARMM36m: an improved force field for folded and intrinsically disordered proteins. Nat. Methods *14*, 71–73. https://doi.org/10.1038/nmeth.4067.
65. Jo, S., Lim, J.B., Klauda, J.B., and Im, W. (2009). CHARMM-GUI Membrane Builder for mixed bilayers and its application to yeast membranes. Biophys. J. *97*, 50–58. https://doi.org/10.1016/j.bpj.2009.04.013.
66. Hess, B., Bekker, H., Berendsen, H.J.C., and Fraaije, J.G.E.M. (1997). LINCS: A Linear Constraint Solver for Molecular Simulations. J. Comput. Chem. *18*, 1463–1472. https://doi.org/10.1002/(SICI)1096-987X(199709)18:12<1463::AID-JCC4>3.0.CO;2-H.

67. Kroon, P.C., Grunewald, F., Barnoud, J., van Tilburg, M., Brasnett, C., de Souza, P.C.T., Wassenaar, T.A., and Marrink, S.-J.J. (2025). Martinize2 and Vermouth: Unified Framework for Topology Generation (ELife Sciences Publications, Ltd.).

68. Nieto, V., Crowley, J., Santos, D., and Monticelli, L. (2023). Birth of an organelle: molecular mechanism of lipid droplet biogenesis. Preprint at bioRxiv. https://doi.org/10.1101/2023.07.28.550987.

69. Lomize, M.A., Pogozheva, I.D., Joo, H., Mosberg, H.I., and Lomize, A.L. (2012). OPM database and PPM web server: resources for positioning of proteins in membranes. Nucleic Acids Res. *40*, D370–D376. https://doi.org/10.1093/nar/gkr703.

70. Wassenaar, T.A., Ingólfsson, H.I., Böckmann, R.A., Tieleman, D.P., and Marrink, S.J. (2015). Computational Lipidomics with insane: A Versatile Tool for Generating Custom Membranes for Molecular Simulations. J. Chem. Theory Comput. *11*, 2144–2155. https://doi.org/10.1021/acs.jctc.5b00209.

71. Pogozheva, I.D., Armstrong, G.A., Kong, L., Hartnagel, T.J., Carpino, C.A., Gee, S.E., Picarello, D.M., Rubin, A.S., Lee, J., Park, S., et al. (2022). Comparative Molecular Dynamics Simulation Studies of Realistic Eukaryotic, Prokaryotic, and Archaeal Membranes. J. Chem. Inf. Model. *62*, 1036–1051. https://doi.org/10.1021/acs.jcim.1c01514.

72. Evans, E., Heinrich, V., Ludwig, F., and Rawicz, W. (2003). Dynamic tension spectroscopy and strength of biomembranes. Biophys. J. *85*, 2342–2350. https://doi.org/10.1016/S0006-3495(03)74658-X.

73. Hub, J.S., de Groot, B.L., and van der Spoel, D. (2010). g_wham—A Free Weighted Histogram Analysis Implementation Including Robust Error and Autocorrelation Estimates. J. Chem. Theory Comput. *6*, 3713–3720. https://doi.org/10.1021/ct100494z.

74. Gapsys, V., de Groot, B.L., and Briones, R. (2013). Computational analysis of local membrane properties. J. Comput. Aid. Mol. Des. *27*, 845–858. https://doi.org/10.1007/s10822-013-9684-0.

Please cite this article in press as: Hu et al., Mechanism of lipid transfer by bridge-like protein VPS13A and the scramblase XK, Cell (2026), https://doi.org/10.1016/j.cell.2026.05.027

STAR★METHODS

KEY RESOURCES TABLE

REAGENT or RESOURCE	SOURCE	IDENTIFIER
Antibodies		
Rabbit monoclonal anti-calmodulin	MedChemExpress	Cat# HY-P82082; RRID:AB_3104023
Bacterial and virus strains		
Competent Escherichia coli DH5a	New England Biolabs	Cat# C2987H
Chemicals, peptides, and recombinant proteins		
cOmplete™, EDTA-free Protease Inhibitor Cocktail	Roche	Cat# 11873580001
TCEP hydrochloride	Hampton Research	Cat# HR2-801
Anti-FLAG M2 affinity gel	Millipore	Cat# A2220
3XFAG peptide	APExBIO	Cat# A6001
GDN	Anatrace	Cat# GDN101
Amphipol A8-35	Anatrace	Cat# A835
DOPC	Avanti Research	Cat# 850375C
DOPE	Avanti Research	Cat# 850725C
DOPS	Avanti Research	Cat# 840035C
Cholesterol (ovine)	Avanti Research	Cat# 700000P
NBD-PE	Avanti Research	Cat# 810153C
Sodium dithionite	Sigma Aldrich	Cat#157953-5G
OptiPrep	Sigma-Aldrich	Cat# D1556
Deposited data		
Cryo-EM map of VPS13A/Nt-CaM	This paper	EMDB: EMD-72912
Cryo-EM map of VPS13A central bridge-domain	This paper	EMDB: EMD-72909
Cryo-EM map of VPS13A/Ct-XKR1	This paper	EMDB: EMD-72913
Model of VPS13A/Nt-CaM	This paper	PDB: 9YG4
Model of VPS13A central bridge-domain	This paper	PDB: 9YFW
Model of VPS13A/Ct-XKR1	This paper	PDB: 9YG5
Experimental models: Cell lines		
Expi293FTM cells	GibcoTM	Cat# A14527; RRID:CVCL_D615
Recombinant DNA		
pCAG-VPS13A-3xFlag	This paper	N/A
pCAG-VPS13A-ΔATG2_C	This paper	N/A
pCMV-3xFLAG-XKR1	Adlakha et al.[9]	N/A
pCMV-3xFLAG-XKR1-PH	This paper	N/A
Software and algorithms		
UCSF ChimeraX	Meng et al.[20]	https://www.cgl.ucsf.edu/chimerax/
Pymol (v.3.1.0)	The PyMOL Molecular Graphics System, Version 3.0 Schrödinger LLC	https://www.pymol.org
AlphaFold3	Abramson et al.[56]	https://alphafoldserver.com.
DeepMainMast	Terashi et al.[21]	https://em.kiharalab.org/algorithm/DeepMainMast
Coot (v.0.9.8.8)	Emsley et al.[19]	https://www2.mrc-lmb.cam.ac.uk/personal/pemsley/coot/;
Phenix (v.1.21.1)	Liebschner et al.[22]	https://phenix-online.org

(*Continued on next page*)

Please cite this article in press as: Hu et al., Mechanism of lipid transfer by bridge-like protein VPS13A and the scramblase XK, Cell (2026), https://doi.org/10.1016/j.cell.2026.05.027

Continued

REAGENT or RESOURCE	SOURCE	IDENTIFIER
Fiji (v.2.16.0)	Schindelin et al.[57]	https://imagej.net/software/fiji/
CryoSPARC (v.4.6.2)	Punjani et al.[58]	https://cryosparc.com
Graphpad Prism (v.10.1.1)	GraphPad Prism	https://www.graphpad.com
GROMACS	Abraham et al.[59]	https://www.gromacs.org
VMD	Humphrey et al.[60]	https://www.ks.uiuc.edu/Research/vmd
Other		
ExpiFectamineTM 293 Transfection Kit	GibcoTM	Cat# A14525
Expi293TM Expression Medium	GibcoTM	Cat# A1435102
UltraAuFoil R1.2/1.3 300 mesh Au grids	Quantifoil	Cat# N1-A14nAU30-50

EXPERIMENTAL MODEL AND STUDY PARTICIPANT DETAILS

Bacterial strain

E. coli DH5a competent cells (#C2987H, New England Biolabs) were used for molecular cloning.

Cell lines

Expi293F^{TM} (#A14527; Gibco^{TM}) cells were used for transient transfection for protein expression. Cells were maintained in Expi293 expression medium (#A1435102, Gibco^{TM}) at 37°C and 8% CO2 under shaking conditions according to the manufacturer's instruction.

METHOD DETAILS

Protein expression and purification

To purify VPS13A protein, the codon-optimized VPS13A gene was cloned into a pCAG expression vector containing a C-terminal 3xFLAG tag. For the VPS13A ΔATG2_C mutant construct, the region encoding the ATG2_C motif (amino acid residues 2866-3029) was deleted from the full-length VPS13A sequence. The resulting truncated construct was cloned into the same pCAG vector backbone. The appropriate plasmid construct was transfected into Expi293 cells with ExpiFectamine (Gibco), following manufacturer's instruction. 48h post transfection, cells were harvested, resuspended in lysis buffer A (50mM HEPES, pH7.4, 300mM NaCl, 1mM TCEP, 10% glycerol, 0.1% Triton X-100) supplemented with protease inhibitor cocktail (Roche). The suspension was incubated on a rotary shaker at 4°C for 15min, followed by mechanical lysis using a Dounce homogenizer (15-20 passes). The crude lysate was centrifuged at 39,191g for 30min at 4°C to remove cell debris. The supernatant containing the extracted protein was incubated with pre-washed anti-FLAG resin (#A2220, Millipore) for 2h at 4°C. The resin was then washed three times with buffer B (50mM HEPES pH7.4, 300mM NaCl, 1mM TCEP, 10% glycerol), followed by incubation in buffer B supplemented with 2mM $MgCl_2$ and 1mM ATP at 4°C overnight to remove chaperone. After three additional washes with buffer B, the bound protein was eluted from the resin using 0.25 mg/mL 3xFLAG peptide (APExBIO) in buffer B supplemented with protease inhibitors. The eluted protein was concentrated through a 100 kDa molecular weight cutoff Amicon centrifugal filter and analyzed by SDS-PAGE stained with Coomassie blue. Calmodulin (CaM) co-purified with VPS13A, resulting in a native VPS13A/CaM complex.

The expression and purification of 3XFLAG-XKR1 was performed as previously described[9] with slight modifications. To make a 3XFLAG-XKR1-PH fusion construct, the region encoding the VPS13A PH domain (amino acids residues 3031-3174) was fused to the C-terminus of XKR1. The resulting construct was cloned into the same pCMV vector with a N-terminal 3xFLAG. Expi293 cells were transfected with plasmids encoding XKR1 or the XKR1-PH fusion construct, and were harvested 48h post transfection. Cell pellets were resuspended in lysis buffer C (50mM HEPES, pH8, 200mM NaCl, 1mM TCEP, 10% glycerol) supplemented with protease inhibitors and lysed using a Dounce homogenizer. To extract XKR1 from membrane, GDN (Anatrace) was added to the lysate to a final concentration of 1.5%, followed by incubation on a rotary shaker at 4°C for 1.5 hours. The lysate was then clarified by centrifugation, and the supernatant was incubated with anti-FLAG resin pre-washed with buffer C containing 0.02% GDN. The remaining purification steps followed the protocol used for VPS13A, with 0.02% GDN included throughout. The final XKR1 protein was concentrated using a 10kDa molecular weight cutoff Amicon centrifugal filter and quantified by Coomassie blue staining using BSA standards.

To allow formation of VPS13A/CaM-XKR1 complex, an excess amount of XKR1 was incubated with purified VPS13A/CaM for 30min at room temperature. The mixture was then loaded onto a Superose 6 Increase 10/300 GL size-exclusion chromatography (SEC) column (GE Healthcare) pre-equilibrated with sample buffer (50mM HEPES, pH8, 200mM NaCl, 1mM TCEP, 0.02% GDN). Peak fractions corresponding to the VPS13A/CaM-XKR1 complex were pooled (Figure S1A), concentrated using a 100 kDa Amicon centrifugal filter, analyzed by SDS-PAGE and used for cryo-EM grid preparation.

Please cite this article in press as: Hu et al., Mechanism of lipid transfer by bridge-like protein VPS13A and the scramblase XK, Cell (2026), https://doi.org/10.1016/j.cell.2026.05.027

Cryo-EM sample preparation and data collection

Freshly purified VPS13A/CaM-XKR1 complex was concentrated to 2.5-3.5mg/mL and supplemented with 0.1% Amphipol A8-35 (Anatrace) prior to grid preparation. A volume of 3.5μL of the complex was applied to a glow-discharged UltraAuFoil R1.2/1.3 300 mesh gold grids (Quantifoil), then plunge-frozen in liquid ethane using an FEI Vitrobot mark IV (Thermo Scientifc) under 100% humidity at 8°C, with a blot force of 1 and blot time of 3s.

Data collection was carried out on a 300-kV FEI Titan Krios G2 transmission electron microscope equipped with a K3 summit direct detection camera at the Yale CryoEM Resource. A total of 26434 micrographs were collected in super-resolution mode at a nominal magnification of 105k (0.832 Å/physical pixel), and each movie was recorded with a total exposure of 1.4s fractionated into 50 frames for a total dose of 50 $e^{-}/Å^{2}$ and with a defocus range of -0.8 to -2 μm.

Image processing

Raw micrographs were imported into CryoSPARC (v4.6.2) for processing (Figure S2). Beam-induced motion was corrected using the Patch Motion Correction algorithm with a Fourier cropping factor of 1/2, and defocus values were estimated using Patch CTF Estimation with default parameters. Micrographs with a CTF fit resolution worse than 6Å were excluded from downstream processing.

Initial 2D templates were derived from blob picking followed by two rounds of 2D classification. A subset of 1662 micrographs was then used for template picking and 669,210 particles of box size 672 pix with 4x Fourier cropping were extracted. After further 2D classification, 101,081 particles were selected to generate a primary 3D reference volume using *ab initio* reconstruction. To obtain an improved reference volume, a larger dataset of 3,814,669 particles from 13,751 micrographs were subjected to three rounds of heterogeneous refinement, using the initial reference and four additional "junk" volumes. This workflow yielded 287,147 unbinned particles, which produced a 3.85Å map via non-uniform (NU) refinement. The resulting volume was subsequently used for 2D classification and selection of 2D templates with a broader range of projected views.

Using the full dataset comprising 25,832 micrographs, particles obtained from template picking were subjected to 2D classification and two rounds of heterogeneous refinement, using the 3.85 Å reference volume and 4 "junk" volumes. Following refinement, approximately 1million unbinned particles were re-extracted and used for *ab initio* reconstruction. Using default *ab initio* settings with 4 classes, followed by heterogeneous refinement, 464,055 particles were selected for NU refinement, yielding a 3.41Å map focused on VPS13A/CaM complex. To resolve the VPS13A-XKR1 complex, the same particle set was subjected to *ab initio* reconstruction with the following settings: 4 classes, maximum resolution of 4 Å, initial resolution of 12 Å, and initial and final minibatch size of 500. After three rounds of heterogeneous refinement, a class of 385,639 particles centered on VPS13A-XKR1 were subjected to NU refinement, resulting a 3.46 Å map. Local refinements were subsequently performed to obtain focused maps of the VPS13A N-terminal region bound to CaM (VPS13A/Nt-CaM), the central bridge-domain, and the C-terminal region of VPS13A in complex with XKR1 (VPS13A/Ct-XKR1).

To analyze conformational heterogeneity of the C-terminal region of VPS13A, a focused 3D classification was performed using a manually created mask around the C-terminus. 3D variability analysis (3DVA) was also conducted with the filter resolution set to 6 Å, using a "simple" output mode with 20 frames to visualize structural dynamics.

Model refinement and validation

The initial model of VPS13A, XK-PH(VPS13A) complex, and VPS13A/Nt-CaM complex were predicted using AlphaFold 3 (https://alphafoldserver.com)[56] then subjected to rigid body fitting in UCSF ChimeraX,[20] followed by a deep-learning-based model rebuilt and fitting using DeepMainmast,[21] except that the VPS13A VAB domain (residues 1876-2504) was refined further due to low resolution. The models were then manually readjusted in Coot[61] against corresponding focused maps derived from local refinement, followed by real space refinement in Phenix.[22]

The following regions of VPS13A (1-33,50-53,128-139, 415-457, 609-625, 794-875, 898-902, 1015-1045, 1192-1201, 1342-1387, 1532-1549, 1671-1715, 1810-1827, 1867-2517, 2731-2764, 2784-2820,2832-3030, 3170-3174), XKR1 (267-269,388-444) and CaM (residues 1 and 149) were not modelled, as the corresponding densities were not visible or at low resolution in all the maps. Representative densities for different parts of the VPS13A/CaM-XKR1 complex are shown in Figure S2.

Molecular graphics were prepared using UCSF ChimeraX[62] and PyMOL (The PyMOL Molecular Graphics System, Version 3.0 Schrödinger LLC).

Liposome preparation and flotation assay

To prepare liposomes, a lipid mixture containing 30% DOPC, 27.5% DOPE, 12% DOPS, 30% cholesterol, 0.5% NBD-PE (all in chloroform) was dried under a gentle N2 stream to a thin film, followed by vacuum desiccation overnight. The dried lipid film was rehydrated in buffer containing 50mM HEPES (pH7.4) and 200mM NaCl to a final lipid concentration of 5mM. The lipid suspension was incubated at 37°C for 1h and then subjected to 10 cycles of flash freeze-thaw. Crude liposomes were extruded 21 times through a 200 nm polycarbonate filter using a mini extruder (Avanti) to yield uniform vesicles.

To analyze liposome binding of VPS13A and the ΔATG2_C mutant, proteins were purified from Expi293 cells as described above. ~2 μg of protein were incubated with 100μL 2.5mM liposome for 30min at room temperature. The mixture was adjusted to 30% OptiPrep by adding an equal volume of 60% OptiPrep (D1556, Sigma-Aldrich) and overlaid with 180μL 15% OptiPrep and 180μL reconstitution buffer (50mM HEPES, pH7.4 and 200mM NaCl) in a 0.8mL ultracentrifugation tube. After centrifugation (SW55Ti,

35,000 rpm, 1h, 16°C), the liposome-containing fraction at the 0%|15% interface was collected, and the liposome-bound proteins were analyzed by SDS-PAGE.

Scrambling assay

Proteoliposomes, containing either XKR1 or the XKR1-PH fusion construct, were prepared as previously described[42] with minor modifications. Fusing the PH domain to the XKR1- C-terminus rather than adding soluble VPS13A or the PH domain to XKR1-containing liposomes had two rationales: (i) since the XKR1 C-terminus is on the same side of the membrane as the regulatory pocket, this ensures that the PH domain can access the regulatory pocket irrespective of XKR1's orientation after reconstitution into the liposome membrane and (ii) the fusion ensures that there are no XKR1s in a PH-domain-free form. The protein:lipid ratios used in the XKR1 and XKR1-fusion construct reconstitutions were comparable, resulting in 20-40 proteins per liposome. Briefly, 180μL of 2.5mM liposomes (30% DOPC, 27.5% DOPE, 12% DOPS, 30% Cholesterol, 0.5% NBD-PE, as above) were mixed with 0.3% Triton X-100 for 30min at 37°C to partially solubilize the lipid bilayer. Subsequently, 20μL of concentrated protein (100-150 ng/ μL) was added and incubated for 1h at room temperature. Detergent was then removed by sequential addition of pre-washed Bio-Beads (Bio-Rad): 20mg for 1h at RT, followed by another 20mg for 1h at RT, and finally 40mg overnight at 4°C. Reconstituted proteoliposomes were then purified via OptiPrep flotation assay as described above.

To analyze lipid scrambling activity, 5μL proteoliposomes were added to 95μL of assay buffer (50mM HEPES, pH7.4, 200mM NaCl, 1mM TCEP) in a white 96-well plate (Corning). Each condition was measured in triplicate. NBD fluorescence was recorded at 30° C using a plate reader (BioTek) with excitation/emission set to 460/538nm. After signal stablization, 5μL freshly prepared dithionite was added to a final concentration of 5 mM to initiate quenching of externally exposed NBD-lipids. Fluorescence was monitored for 10 min,followed by addition of 5μL of 10% Triton X-100 and 5μL dithionite to fully quench remaining fluorescence.

System setup and simulation details

The starting structure of the VPS13A/CaM-XKR1 complex for both AA- and CG-MD simulations was taken from the cryo-EM refined structure. Missing loops in the structure were modelled using Modeller.[63] The loop comprising residues 1671-1715 and the ATG2_C domain were aligned from the AlphaFold prediction,[18,56] and the disordered ATG2_C domain was subsequently manually displaced from its initial position under the C-Cap of VPS13A. The complex was minimized in vacuum using the CHARMM36m force field[64] before running any AA- or CG-MD simulation. Both AA- and CG-MD simulations were carried out using the software GROMACS.[59]

AA-MD Simulations

The CHARMM-GUI Membrane Builder[65] was used to prepare the AA systems, with the membrane compositions listed in Table S2. Each system was solvated with CHARMM TIP3P water and ionized with 150 mM of NaCl or KCl and neutralizing Na^+/K^+ or Cl^- ions. For all AA-MD simulations, the detailed description of lipid composition, system size and simulation time are collected in Table S2, The CHARMM36m force field was used.[64] The CHARMM-GUI protocol for minimization and equilibration was followed for each system, which consists in an energy minimization using the steepest descent algorithm followed by two NVT equilibrations and four NPT equilibrations with positional restraints on both the protein backbone and the phosphate atom of each lipid that are increasingly removed. The equilibration runs used the v-rescale thermostat and the C-rescale semi-isotropic barostat to maintain the temperature at 310 K and the pressure at 1 bar. The v-rescale thermostat, with separate coupling for the protein, the membrane, and the ionized solvent, and a coupling time constant of 1.0 ps, was used to keep the system at 310 K during the production runs. The pressure of 1.0 bar in the productions runs was kept with the semi-isotropic C-rescale barostat, with a compressibility of $4.5 \cdot 10^{-5}$ bar, and a coupling time constant of 5.0 ps. For the electrostatics, the Particle Mesh Ewald method was used to compute the electrostatic interactions, with a Fourier spacing of 0.12 nm and a cutoff of 1.2 nm. Van der Waals interactions were switched to zero over the 1-1.2 nm range. The LINCS algorithm was used to constrain the bonds involving hydrogen atoms.[66] Frames were written every 100 ps, with a time step of 2 fs.

CG-MD Simulations

All CG-MD simulations were performed using the MARTINI 3 force field.[40] The atomistic structure of the protein complex was converted to a CG model using the Martinize2 script.[67] An elastic network with a force constant of 700 kJ mol^{-1} nm^{-2}, with an upper elastic bond cutoff of 0.9 nm, was used to restrain the secondary structure of the protein and the protein-protein interfaces. To reproduce the expected mobility of certain regions of the protein, the elastic network was removed from i) all loops, ii) between the ATG2_C domain and the rest of the protein, iii) between the two helices at the C-terminal region (residues 2790-2810, and 2839-2856) and the rest of the protein.

To fill the hydrophobic cavity of the protein with 54 lipids, the unbiased CG-MD protocol for iterative lipid binding from[26] was followed, after aligning the published Vps13 structure with 49 lipids inside. To oversaturate the cavity with more lipids, we adapted a recently proposed *in silico* lipid synthesis protocol[68] which consists of the following iterative steps: *i*) Duplicating one of the lipids inside the cavity, ii) Slow-growth simulation of the duplicated lipid to avoid clashes, and iii) Standard equilibration + production for 50 ns.

The orientation in the membrane for the proteins was computed using PPM,[69] and the CG structure was embedded in a lipid bilayer using the Insane script.[70] The plasma membrane-like lipid composition was adapted from.[71] The systems were solvated and ionized with 150 mM NaCl; additional Na^+ or Cl^- ions were added to neutralize the charge of each system. Description of all simulations details (lipid composition, system size, simulation time, etc.) are collected in Table S3.

Please cite this article in press as: Hu et al., Mechanism of lipid transfer by bridge-like protein VPS13A and the scramblase XK, Cell (2026), https://doi.org/10.1016/j.cell.2026.05.027

The standard minimization and equilibration protocol from CHARMM-GUI was used for each system, which consists of an initial minimization using the steepest descent algorithm followed by six equilibrations with positional restraints on both the protein backbone beads and the lipid headgroups, which were gradually removed. The time step was initially fixed at 1 fs and gradually increased until 20 fs. The equilibration runs used the v-rescale thermostat and C-rescale barostat to maintain the temperature at 310 K and the pressure at 1 bar. For production, three independent replicas were run for at least 10 microseconds (all simulations times are listed in Table S3) for each system using a time step of 20 fs. The v-rescale thermostat, with separate coupling for the protein, the lipids, and the ionized solvent, and a coupling time constant of 1.0 ps, was used to maintain the temperature at 310 K during production. The semi-isotropic Parrinello-Rahman barostat, with a compressibility of $3*10^{-4}$ bar, a coupling time constant of 12 ps, and a 10-step frequency for the coupling was used to control the pressure at 1.0 bar during production runs. Electrostatic interactions were computed using the reaction-field electrostatics approach with a cut-off of 1.1 nm. Van der Waals interactions were computed using a cut-off 1.1 nm along with a potential-shift-Verlet scheme. The neighbor list was updated every 20 steps using the Verlet list scheme.

Membrane Tension Simulations

For the AA-MD and CG-MD simulations with tension on the membrane, NPT simulations with the C-rescale barostat and *surface-tension* as pressure coupling type were used, taking 1 bar on the z direction, and either 400 bar nm (20 mN m^{-1}), 300 bar nm (15 mN m^{-1}), or 200 bar nm (10 mN m^{-1}) on the x/y dimensions of the box (all details on the systems are described in Tables S2 and S3). These settings allow the bilayer to expand laterally, resulting in higher area-per-lipid, and they are within the range of membrane tensions before membrane rupture occurs experimentally.[72]

Umbrella-sampling simulations

Potential of Mean Force of lipid translocation in AA simulations. The reaction coordinate used to compute the free energy associated to the phospholipid translocation mediated by XKR1 was used as the distance along the z-axis between the nitrogen atom from a selected phospholipid and the center-of-mass (COM) of the side chains of four residues located at the extracellular side of the interface between TM1-TM4 (Tyr28 from TM1, Trp36 from TM2, Gln162 from TM3, and Arg169 from TM4). The initial configuration used to start the pulling corresponded to the conformation of XKR1 that presented the highest value for the distance between TM1-TM4, as obtained from our unbiased AA-MD simulations. Then, two slow pulling simulations were carried out. During the first pulling a selected phospholipid (located at the cytosolic entrance of the interface between TM1-TM4) was pulled for 1 μs with a rate of ~3.7 nm/μs and a force constant of 3000 kJ mol^{-1} nm^{-2}. Then a second pulling was carried out for the same lipid in the backward direction. A total of 78 umbrella windows were extracted from these two pullings, ranging from -3.7 nm until 0.2 nm and spacing of 0.1 nm. Each window was simulated for a total of 300 ns, with a force constant of 1000 kJ mol^{-1} nm^{-2}. The respective free energy profile was recovered using the Weighted histogram Method (WHAM) with 100 bootstrap iterations to assess the statistical variance (http://membrane.urmc.rochester.edu/content/wham).

Potential of Mean Force of lipid delivery in CG simulations. The reaction coordinate used to compute the free energy profile for the delivery of a lipid from VPS13A into the donor membrane was taken as the distance between the COM of the delivered lipid along the bilayer normal (z) to the z coordinate of the membrane center, which was calculated as the COM of all lipids contained within a cylinder of 2.0 nm radius around the COM of the delivered lipid. The windows were spaced at 0.1 nm, with a distance range between 1.2 and 4.5 nm. Each window was simulated for 505 ns, using a harmonic force constant of 500 kJ mol^{-1} nm^{-2}. The first 205 ns were not considered, and the PMF was constructed using WHAM[73] as implemented by GROMACS. Convergence was tested by computing the PMF in 100 ns blocks after discarding the first 5 ns. The windows were selected from an initial pulling simulation along the reaction coordinate, using a force constant of 1000 kJ mol^{-1} nm^{-2} and a pulling rate of $2{\cdot}10^{-5}$ nm ns^{-1}.

MD simulations analysis

The opening of the interface between TM1 and TM4 from XKR1 were traced by measuring the distance between the carbon-α from the amino acids Thr27 and Val167. Distances were computed with the gmx distance tool. Data points were stored every 0.5 ns.

The area per lipid was computed taking frames every 1 ns using the g_lomepro tool,[74] and using the phosphorous atom for each lipid.

The density of the different groups (water, phosphate groups of the membrane, RBG lipids, C-cap of VPS13A) along the z coordinate was calculated using the gmx density tool. When specified, the densities were normalized so they integrate to 1. For systems where lipid delivery is observed, simulation time between 1 μs and the time at which bulk lipid delivery happens was used.

Lipid scrambling was quantified by tracking the tilt angles (θ) of each lipid with respect to the membrane plane normal throughout the simulation, following the same protocol as in.[42] Here, a flip (movement from the upper to the lower leaflet) or flop (movement from the lower to the upper leaflet) event was considered when the lipid exhibited a change to tilt angles $\theta \geq 130^{\circ}$ or $\theta \leq 50^{\circ}$, respectively. The angles were computed every nanosecond with the gmx gangle tool, and events were reported as events/μs, omitting the first 2 μs for equilibration. The main amino acids involved in the lipid scrambling were obtained by calculating the interactions between the protein and the scrambled lipids. For this, an interaction was considered when the distance between any aminoacid bead of the protein and the headgroup or the phosphate beads of the scrambled lipid was equal to or less than 0.45 nm.

The membrane insertion depth of the protein was calculated by measuring all pairwise distances between VPS13A beads and lipid glycerol beads of the membrane. Then, for each time frame, and only considering the glycerol beads within 2.0 nm of the protein, i) the maximum (in absolute value) z-position of the protein beads and ii) the mean z-coordinate of the selected glycerol lipid beads were stored and subtracted to get the maximum membrane insertion depth of the protein per frame.

Please cite this article in press as: Hu et al., Mechanism of lipid transfer by bridge-like protein VPS13A and the scramblase XK, Cell (2026), https://doi.org/10.1016/j.cell.2026.05.027

Root Mean Square Fluctuation (RMSF) was calculated using the gmx rmsf tool and using the backbone beads of the protein.

Membrane thinning was analyzed using python scripts with libraries MDAnalysis, Numpy and SciPy. MD trajectories were initially fitted to the backbone beads of the transmembrane part of the systems on x and y directions. Next, for each frame the z-coordinates of the phosphate beads were stored. The membrane thickness was obtained by subtracting the z-coordinates of the inner leaflet from the z-coordinates of the outer leaflet. The z-coordinates of the phosphate beads corresponding to the cytosolic leaflet were also used to compute membrane curvature, by subtracting the z coordinate of each bead and the average z coordinate of the entire leaflet for each frame. The results of both membrane thickness and curvature were averaged using a grid along x and y with a size of 0.1 nm.

The minimum distance between the membrane and the lipids inside the bridge-domain of VPS13A was computed using the gmx mindist tool.

To count the number of lipids delivered, the distance along z between a terminal lipid tail bead of the POPC lipids (C4A) to the membrane center was computed for each frame. Noise was reduced by applying a block averaging technique every 10 ns. A lipid is considered as delivered when the averaged distance is less than 2.3 nm.

The rate of lipid delivery was computed from the average over the three replicas, as the inverse of the time for lipid delivery. Error bars were computed as the standard deviation of the time for lipid delivery from the three independent simulations. For simulations where no lipid delivery was observed, the error bars were given as the inverse of the total simulation time.

Visualization of the trajectories and rendering were done using VMD.[60]

QUANTIFICATION AND STATISTICAL ANALYSIS

For biochemical liposome flotation assay, statistical analyses were performed in GraphPad Prism (v.10.1.1). Quantification from three independent experiments is shown as mean ± SD. Statistical analysis was performed using an unpaired Welch's t-test. Significance was indicated with asterisks (**** $P < 0.0001$).

For molecular dynamics simulations, statistical analyses were performed in Python using the Numpy, Pandas and Statsmodels libraries. For all simulations three independent replicas were performed ($n = 3$). A one-way analysis of variance (ANOVA) was applied, followed by Tukey's honestly significant difference post hoc tests to perform pairwise comparisons between all groups, with a pure plasma membrane-like system as negative control. Significance was indicated with asterisks (***$p \leq 0.001$, **$p \leq 0.01$ and *$p \leq 0.05$).

Quantification and analysis details are described in each relevant section of the methods or figure legends.